A microscale analysis of hydrothermal epidote: Implications for the use of LA-ICP-MS mineral chemistry in complex alteration environments

Ayesha D. Ahmed[1*], Louise Fisher[2], Mark Pearce[2], Angela Escolme[1], David R. Cooke[1], Daryl Howard[3] and Ivan Belousov[1]

[1] Transforming the Mining Value Chain, An ARC Industrial Transformation Research Hub, CODES, University of Tasmania

[2] Commonwealth Scientific and Industrial Research Organisation (CSIRO)

[3] Australian Synchrotron

***Corresponding author: ayesha.geologist@gmail.com**

Abstract

High resolution, quantitative imaging of epidote from the Ann Mason fault block, Yerington district, Nevada, using scanning electron microscopy (SEM), X-ray fluorescence (XRF) and laser ablation inductively coupled plasma mass spectrometry (LA-ICP-MS) has revealed at least two types of epidote (type 1 and type 2), each with different major and trace element chemistry. Type 1 epidote is coarser-grained, typically greater than 50 μm in diameter, and forms euhedral crystals that display twins and sector zones enriched in Fe, Sr, and Mn. Type 2 epidote is finer-grained, typically <30 μm diameter, irregularly zoned with respect to Fe and Al, and forms polycrystalline aggregates that include void space.

Two sources of intragranular compositional variability are defined in this study; one related to different generations of epidote only visible on the microscale; and the other related to crystallographic features such as sector zones and twins. Intragranular compositional variations within Yerington epidotes highlight the potential importance of detailed sample characterization

in complex alteration environments prior to undertaking mineral chemistry studies in the context of resource exploration. Based on statistical analysis of LA-ICP-MS spot data from one sample, the optimal number of spot analyses to adequately represent the range in element concentrations within zoned or twinned crystals is determined to be at least 40.

Introduction

In situ trace element analysis of epidote and chlorite using laser ablation inductively coupled plasma mass spectrometry (LA-ICP-MS) has been used in past studies to extend the detectable hydrothermal alteration footprint around porphyry Cu deposits (e.g., Cooke et al. 2014a; 2014b; Wilkinson et al., 2015; Wilkinson et al., 2017; Baker et al., this volume; Cooke et al., this volume; Wilkinson et al., this volume). This work has shown that trace element dispersion halos recorded by epidote and chlorite can be detected at greater distances than those detected by conventional whole-rock chip sampling. Consequently, mineral chemistry analyses using LA-ICP-MS have the potential to provide explorers with a new suite of geochemical tools to assess both the proximity to, and magnitude of, a porphyry Cu-(Mo-Au) deposit (Cooke et al., 2014a). Other minerals such as zircon, apatite, alunite, muscovite and pyrite has been demonstrated to have similar potential for vectoring and/or fertility assessments (e.g., Ballard et al., 2002; Large et al., 2009; Chang et al., 2011; Dilles et al., 2015; Wilkinson et al., 2015; Lu et al., 2016; Lee et al., 2017; Uribe-Mogollon and Maher, 2018; Alva-Jimenez et al., this volume).

Studies on epidote mineral chemistry have identified that there can be a range in concentrations for a given element within an individual epidote sample, and this range can span orders of magnitude (Cooke et al., 2014a; Pacey et al., 2016). However, the crystallographic sources of this compositional variability within epidote has not been sufficiently investigated. LA-ICP-MS element maps of epidote presented by Cooke et al. (2014a; this volume) did not capture any significant compositional variability and instead showed relatively uniform concentrations of trace elements across an aggregate of epidote grains.

In the Ann Mason fault block, Yerington district, Nevada (Fig. 1), epidote occurs as part of at least three alteration assemblages: (1) magmatic-hydrothermal propylitic alteration (epidote ±

actinolite ± chlorite ± albite ± hematite) related to porphyry Cu mineralization (Dilles and Einaudi, 1992); (2) retrograde skarn alteration (epidote + albite ± calcite ± scapolite; Harris and Einaudi, 1982); and (3) regional sodic-calcic alteration not directly related to porphyry mineralization (epidote + albite ± actinolite ± titanite ± chlorite; Carten, 1986; Dilles and Einaudi, 1992). In this study, we use SEM backscatter images, micro-XRF element maps, LA-ICP-MS raster maps, and LA-ICP-MS spot data to explore microscale geochemical and textural complexity in epidote from in and around the Ann Mason porphyry Cu deposit (Fig. 1). We distinguish between compositional variability associated with crystallographic features and variability resulting from multi-generational composite epidote grains. We evaluate the impact of microscale compositional heterogeneities on the interpretation and successful implementation of mineral chemistry as an exploration tool. The study concludes by proposing best practice guidelines for undertaking mineral chemistry studies in complex alteration environments.

Geology of the Yerington porphyry Cu district

The Yerington porphyry Cu and skarn district is located approximately 120 km southeast of Reno, Nevada, USA (Fig. 1). Porphyry and skarn deposits are associated with the Jurassic Yerington batholith (Fig. 1; Einaudi, 1977; Harris and Einaudi, 1982; Proffett and Dilles, 1984; Dilles, 1987, Dilles and Wright, 1988), a medium to high-K calc-alkaline polyphase intrusive complex (Dilles, 1987). The Yerington batholith intruded a sequence of late Triassic to Jurassic volcanic and sedimentary rocks over a period of approximately one million years (Dilles and Wright, 1988). The batholith is composed of McLeod Hill quartz monzodiorite (169.4 ± 0.4 Ma; Dilles and Wright, 1988), Bear quartz monzonite, and Luhr Hill granite, with associated granite porphyry dikes (168.5 ± 0.4 Ma; Dilles and Wright, 1988). The Shamrock batholith occurs in the southern part of the Yerington district (Fig. 1). It has a monzonitic composition and intruded the same Triassic–Jurassic volcano-sedimentary package at 165.8 ± 0.4 Ma (Dilles, 1987, Dilles and Wright, 1988). Tertiary volcanic rocks cover much of the northern Yerington district. Early Miocene (~17 Ma), large-scale crustal extension resulted in the tilting of major fault blocks 60–90° to the west, exposing vertical cross sections through the district (Proffett, 1977; Proffett and Dilles, 1984).

The Ann Mason porphyry Cu-(Mo-Au) deposit has a combined measured and indicated mineral resource of 4.49 Mt Cu, 84.8 kt Mo, and 37.7 t Au (Kulla et al., 2015). Porphyry Cu-(Mo-Au) mineralization at Ann Mason was associated with the intrusion of the Luhr Hill granite porphyry dikes (Dilles, 1984; Dilles et al., 1992; Dilles and Einaudi, 1992, Dilles et al., 2015). Potassic alteration, consisting of biotite ± K-feldspar, is associated with the main mineralization event (Dilles et al., 1992) and defines a restricted domain in the core of Ann Mason. Sericite alteration, comprising muscovite or illite + pyrite ± quartz ± rutile, occurs above (west of) Ann Mason (Dilles et al., 1992). Epidote and chlorite are part of the propylitic and sodic-calcic alteration assemblages in the district, and have a widespread occurrence (Dilles and Einaudi, 1992). They most likely formed synchronously with potassic alteration but were localized on the fringes of the mineralizing system (Dilles and Einaudi, 1992).

The emplacement of the Yerington batholith resulted in three generalized stages of skarn development (Einaudi, 1977; Einaudi, 1982; Harris and Einaudi, 1982): (1) a metamorphic stage that affected mainly Triassic volcanic rocks and had a negligible effect on the surrounding limestone; (2) an early metamorphic-metasomatic alteration stage that affected all of the Triassic sedimentary rocks, and caused the formation of fine-grained calc-silicate rocks with high garnet to pyroxene ratios; and (3) a late metasomatic stage that formed extensive areas of pyroxene and coarse-grained garnet skarn, associated with Cu-mineralization. Garnet–pyroxene skarn is overprinted by late-stage pervasive epidote alteration and epidote ± albite veins. The Yerington batholith also underwent widespread metasomatism to garnet–pyroxene endoskarn (Einaudi, 1977; Harris and Einaudi, 1982). Skarn mineralogy was poorly developed in the Shamrock batholith as compared to the Yerington batholith (Harris and Einaudi, 1982). Although the Shamrock batholith post-dated porphyry Cu mineralization (Dilles and Wright, 1988), it is spatially associated with a number of Cu skarn deposits including the Casting Copper (0.45 Mt Cu produced; Harris and Einaudi, 1982), and Ludwig deposits (0.18 Mt Cu produced; Harris and Einaudi, 1982; Fig. 1).

Methods

Sample selection

Seven samples from the Yerington district were selected for detailed microtextural and compositional analysis to reflect three main features: (1) the spatial extent of alteration in and around Ann Mason, i.e. deposit proximal vs. deposit distal samples; (2) pre- to syn-mineralization (Yerington batholith) and post-mineralization (Shamrock batholith) rock units; and (3) different styles of epidote alteration, i.e. porphyry-related vs. skarn. Table 1 provides a description of samples used in this study. Sample locations are included in Figure 1 and the samples analyzed are illustrated in Figure 2.

Scanning electron microscopy (SEM)

Samples were analyzed by backscattered electron (BSE) imaging and energy-dispersive X-ray spectrometry (EDS) at the University of Tasmania Central Science Laboratory. All sample preparation was completed at the University of Tasmania lapidary. Samples were cut and set with epoxy into 25 mm-diameter round mounts. Mount locations within each hand sample are illustrated in Figure 2. Petrography was carried out on a Hitachi SU-70 Schottky field emission SEM fitted with an Oxford AZtec XMax80 silicon drift detector EDS system at 5–15 kV accelerating voltage. Spectra from one in-house cobalt standard were collected in addition to three epidote and three chlorite reference spectra from respective in-house standards during each analytical session. Magnification of >300x was maintained during EDS spectra data collection to prevent signal loss along the edges of the detector.

LA-ICP-MS spot analysis and imaging

LA-ICP-MS spot and image data were collected using an Agilent 7900 ICP-MS coupled to an Australian Scientific Instruments Resolution system with 193 nm ArF excimer laser at the CODES LA-ICP-MS Laboratory, University of Tasmania. Laser ablation analyses were performed in an atmosphere of pure He flowing at a rate of 0.35 l/min. Immediately past the ablation point within the cell, He carrier gas was mixed with Ar (1.05 l/min) for improved efficiency of aerosol transport. The ICP-MS instrument was tuned for production of molecular oxide species (i.e. $^{232}Th^{16}O/232Th$) and doubly charged ion species (i.e. $^{44}Ca{+}{+}/^{44}Ca+$) below 0.2%, therefore no correction was applied for interfering species introduced into the analyte signal. However,

possible argide, oxide, and hydroxyl interferences on Ag and Au from Zr, Gd, Hf and Ta were monitored in each analysis.

The laser beam size used was 20–30 µm with a repetition rate of 5 Hz, and a laser energy density of ~3.5 J/cm^2. Each analysis was performed in the time-resolved mode, which involved sequential peak hopping through the mass spectrum. Dwell times on each mass varied between 5 and 50 ms, depending on the count rates. The dwell times were selected to enable detection limits at the level of single mg/kg for trace elements at low concentrations, and at the level of single mg/g for trace elements at high concentrations. The total sweep time (time required to measure all isotopes once) was 0.80 s. The analysis time for each sample was 90 s, comprising a 30 s measurement of the background (laser off) and a 60 s analysis with the laser on.

Spot data reduction was undertaken according to standard methods (Longerich et al., 1996), using Ca as the internal standard element for epidote and using an in-house-developed Excel© spreadsheet. Internal standard element concentrations were calculated based on average values obtained from SEM EDS spectral data where available. NIST612 was used as the primary calibration standard for drift correction and primary calibration; GSD-1G and BCR-2G were used as secondary standards to account for differences in spot size and ablation properties between epidote and the NIST glass standard. The laser beam size for standard analyses was 100 µm for NIST612 and 20–30 µm for GSD-1G matching those of the sample. All three standards were analyzed twice every 1–1.5 hours to monitor drift in sensitivities. Spot locations were selected where sample material appeared most homogeneous, and inclusions of other minerals were not visible. In most cases, sample locations had been characterized texturally and geochemically using SEM prior to LA-ICP-MS analysis.

Between 20 and 28 spots were collected from each sample mount. In order to determine the optimal number of LA-ICP-MS spot analyses to collect for texturally complex samples, 100 spot analyses were collected from a single sample (YE16AA151). Spot data from sample YE16AA151 (n = 100) were randomly ordered using the software package KNIME© in order to remove the effect of any systematic changes in epidote composition along the length of the epidote vein analyzed (Table 1). Individual datapoints were then selected at random from the dataset and the

185 average values plotted (n = 1, 2, 3, …, x) using the method of sampling with replacement at each
186 step increase in spot number. Relative differences between cumulative averages at a given
187 number of analyses and the final average (n = 100) were calculated to evaluate variability.
188
189 Following data collection, time resolved graphs of counts per second data for each analysis were
190 interrogated to identify contamination by other minerals. Part of the analysis was considered to
191 represent a single mineral phase if all elements behaved similar to each other and if the major
192 element constituents (Ca, Fe, Al, Si) occurred at expected count rates. In many cases, the presence
193 of inclusions of other mineral phases could be identified. If the different mineral phases could not
194 be separated, the entire spot was discarded from the data set. If the data corresponding to epidote
195 could be separated from other mineral phases, then the particular time interval was isolated and
196 used in further calculations. Integration periods below 10 s were discarded.
197
198 Images of elemental distributions within epidote grains were acquired by rastering a set of
199 parallel lines across the sample. The laser beam size used for imaging varied between 4 and 6 µm.
200 A repetition rate of 10 Hz was used. Rastering speed was equal to the laser beam size per second.
201 Spacing between the lines was equal to the laser beam size, resulting in full coverage of the
202 desired area of the samples. Each line on the image was pre-ablated to remove surface
203 contamination from previous ablations. Time of acquisition of each image varied between 1.5 and
204 2.5 h. NIST612 was used as the primary calibration standard for drift correction and primary
205 calibration. GSD-1G was used as the secondary standard.
206
207 *X-ray fluorescence microscopy*
208
209 Following LA-ICP-MS analysis, thin sections (30–60 µm-thick) mounted on pure-quartz glass
210 were cut from sample mounts for X-ray fluorescence microscopy (XFM). Pure quartz slides were
211 chosen to minimize background contributions during analysis (Fisher et al., 2015). Micro X-ray
212 fluorescence (micro-XRF) maps were collected on seven samples (Table 1) with the XFM beamline
213 at the Australian Synchrotron, Melbourne, Australia using the Kirkpatrick-Baez mirror
214 microprobe end-station (Paterson et al., 2011) and the Maia 384 detector array using an 18.5 keV
215 incident energy. Experimental setup and methods followed those outlined in Fisher et al. (2015).

Large-scale overview scans (typically 2 cm x 2 cm) were analyzed first at a 6 μm pixel size. Element maps produced from the overview scans were used to select locations for detailed, high-resolution quantitative element mapping (1 μm pixel size). Spectral data were processed and analyzed using the GeoPIXE software suite, which applies a fundamental parameters approach, and it has no constraint for explicit per-element calibration (Ryan 2005, De Boer 1993). Several single element foils, Pt, Fe and Mn, (Micromatter Canada) were analyzed during the experiment for use as references to establish elemental quantification. Spectral deconvolution and image generation were completed using the dynamic analysis method, where a representative total spectrum is fit to the data with a detailed model of Maia detector array efficiency (Ryan, 2000, Ryan et al., 2010a, Ryan et al., 2010b). Spectral fitting used the relative intensities of X-ray lines that reflect integration of yields and X-ray self-absorption effects for the given matrix or mineral phase and the contrasting efficiency characteristics across the detector array (Ryan et al., 2010a, Ryan et al., 2010b; Fisher at al., 2014). Quantitative element maps were generated using an epidote matrix, and therefore the concentrations of elements in other mineral phases can only be considered relative and not quantitative.

Results

Vein morphology

Five samples in this study contained veins (Table 1; Fig. 2). Petrographic analysis by SEM indicate that epidote veins consist dominantly of epidote ± chlorite ± actinolite ± titanite ± pyrite. The veins can be categorized into three discrete morphologies (Figs. 2 and 3): (1) micro-fracture vein meshes—individual veins have a high length to width ratio and are <1 mm wide with irregular margins (Fig. 2C; YE16AA097); (2) irregular—vein margins are jagged, and the boundary between the vein and vein halo is not distinct (Fig. 2E; YE16AA126 and Fig. 2G; YE16AA212); and (3) regular—vein margins are sharp (Figs. 2D and 3B; YE16AA112 and Figs. 2F and 3D; YE16AA151). The alteration halos have similar minerals to the veins: epidote + albite ± chlorite ± actinolite ± titanite ± pyrite (Figs. 2 and 3).

Epidote morphology and chemistry

Two distinct epidote textures were identified in all samples, coarse-grained (type 1) and finer-grained polycrystalline (type 2). SEM backscatter images showing both types of epidote are presented in Figure 4. Both textures occur in replacement (Fig. 4A), skarn (Fig. 4B), and vein samples (Fig. 4C–E). Type 1 epidote crystals are typically >50 μm in diameter, and exhibit poorly developed Fe–Al zonation. Overall, the Fe-content of type 1 epidote, measured by EDS, is higher than type 2 by 1–4 wt % Fe (Fig. 4A, B, E). Type 1 crystals lack inclusions of other minerals. Type 2 epidote commonly occurs in the assemblage epidote ± albite ± chlorite ± quartz. Type 2 epidote are finer grained (<30 μm diameter) and occurs as polycrystalline aggregates along with small pits, voids, and/or inclusions of titanite (Fig. 4E). Type 2 epidote typically occurs in the assemblage epidote ± albite ± chlorite ± titanite ± quartz. In some samples, sharp contacts define the boundary between type 1 and type 2 epidote crystals, where type 2 has enveloped or is intergrown with type 1 (Fig. 4A–D).

Porphyry deposit-proximal samples: Sample YE16AA151 contains a 100 μm-wide epidote vein with a small 30 μm-wide splay in epidote–chlorite-altered quartz monzodiorite (Figs. 2F and 3D). This sample has a well-developed epidote–albite halo surrounding a thin (<250 μm-wide) epidote vein. Micro-XRF overview element maps (6 μm pixel size; Fig. 5) show that Sr is concentrated in epidote relative to other minerals, both within the vein and in fine-grained disseminated epidote in the 1–2 cm-wide vein halo (Fig. 5C). The extents of the epidote–albite vein halo is coincident with elevated Fe and Mn, which is concentrated in disseminated epidote (Figs. 5B and D). Manganese and Fe are more concentrated in amphibole than epidote. Base metals such as Cu (Fig. 5E) and Zn (Fig. 5F) are not detectable in epidote, either in the veins or vein halos. These elements are instead concentrated in actinolite, hornblende, and/or chlorite, where detected.

Figure 6A–F shows high resolution quantitative micro-XRF element maps from YE16AA151. The monomineralic epidote vein is surrounded by a vein halo of actinolite and chlorite with minor titanite. The main vein segment can be divided into three zones based on compositional differences (Fig. 6A). Zone 1 is defined as the vein margin. It is located adjacent to the wall rock and contains elevated Fe (12 wt % Fe; Fig. 6D). Zone 2 is located at the vein center. It is characterized by coarse-grained epidote with elevated Sr (>1.5 wt % Sr), and As (50–150 ppm). Zone 2 contains elevated Mn (0.1 wt %) compared to zone 1 (<0.1 wt % Mn). Zone 3 is also located

in the vein center and has elevated Mn as compared to the other two zones, but lower Fe (10 wt %) and Sr (1 wt %) than zone 1. Zone 2 contains lower Mn than zone 3 (0.3 wt % Mn). Zone 1 contains higher Fe than zones 2 and 3 (9–11 wt % Fe). Epidote from zone 1 is intergrown with epidote from zones 2 and 3 (Fig. 6A). Copper is below detection limit in all three epidote veins. Quantitative differences in copper content between vein epidote and wall rock minerals cannot be determined because XRF spectra were fitted for epidote only. However, Cu is enriched in wall rock minerals (chlorite and actinolite), particularly along interpreted cleavage planes, relative to the epidote vein (Fig. 6E).

Porphyry deposit distal samples: Overview micro-XRF scans of distal sample YE16AA126 show a 0.7 cm-wide zone of irregular epidote veins with a series of thin epidote veinlets oriented at 45° to the main vein zone (Fig. 5G–I). Both the main epidote vein zone, and epidote veinlets are associated with elevated Sr and Co compared to other minerals (Fig. 5H–I). Manganese is more concentrated in actinolite than epidote (Fig. 5H).

High resolution micro-XRF maps for part of distal sample YE16AA126 are provided in Figure 7D–G. These images highlight variations across the main epidote alteration zone (Fig. 5G). Epidote occurs with titanite, actinolite and chlorite (Fig. 7D). Copper is concentrated in chlorite relative to epidote (Fig. 7E; typically <0.001 wt % Cu in epidote). Euhedral laths of epidote (potentially type 1 epidote) have elevated Mn (Fig. 7F) and Sr (Fig. 7G) concentrations relative to finer grained aggregates of type 2 epidote.

Shamrock batholith samples: High resolution micro-XRF maps of epidote samples from the Shamrock batholith are presented in Figure 6G–L. The epidote vein in sample YE16AA112 shows both textural and compositional changes from the vein wall to the vein center. Epidote closest to the vein wall in sample YE16AA112 occurs as fine-grained anhedral aggregates while epidote in the center of the vein is coarser-grained, and subhedral, showing elongation along one axial direction (Fig. 6I). The mineralogy is different between the fine-grained and coarse-grained zones. Chlorite is absent from the outer, fine-grained part of the vein, as shown by the absence of Mn in Figure 6G. Although As values are generally low overall (<100 ppm), As values are higher in the center of the vein (<150 ppm) compared to the vein margin (<50 ppm; Fig. 7H).

At the hand-sample scale (Fig. 2C), sample YE16AA097 contains a 2–3 cm-wide zone of intense epidote–albite alteration. Overview scan micro-XRF images (Fig. 5J–L) highlight a network of epidote veinlets connecting zones of epidote replacement. Veinlets are on the order of 200–300 μm wide (Figs. 5J and 6J). Amphibole has been destroyed in the area around the vein network, as shown by the absence of Zn (Fig. 5L). High resolution micro-XRF maps show that where the vein has intersected a Ca-bearing mineral (i.e. actinolite or calcic plagioclase), that wall rock mineral has been altered to epidote (Fig. 6J–L). Replacement epidote has higher Fe (12 wt % Fe; Fig. 6J) and Sr than vein epidote (9–12 wt % Fe) in this sample. Replacement epidote has more variable and lower As contents than vein epidote.

Skarn sample: Sample YE16AA063 contains the coarsest-grained epidote of all seven samples analyzed, with crystals up to 1 mm in diameter (Figs. 3A and 7A–C). Variations in the concentrations of Sr, Mn, and Fe in epidote are visible in both micro-XRF (Fig. 7A–B) and LA-ICP-MS maps of this sample (Fig. 8A and C). Euhedral crystals of type 1 epidote have overall higher Fe than fine-grained aggregates of type 2 epidote (Figs. 7 and 8). Micro-XRF maps highlight sector zones in type 1 epidote whereby Sr and Fe are preferentially incorporated into specific crystal faces (Fig. 7A). Sector zones were not observed in type 2 epidote, possibly due to the resolution of the XRF map. LA-ICP-MS maps show that in addition to major components of epidote (Fe, Mn, Sr) the trace elements As, Sb, and Ce are higher in type 1 epidote compared to type 2 (Fig. 8). Cerium is enriched in thin (<5 μm) repetitive bands on the edge of type 1 epidote (Fig. 8F).

Variations in epidote composition with lateral distance from Ann Mason

Variations in epidote compositions as a function of distance from the center of Ann Mason are illustrated in Figure 9. Proximal epidote samples contain higher mean concentrations of Sr (approximately 8,000 ppm and 4,500 ppm, respectively) than distal epidote (<3,000 ppm), skarn epidote (~3,000 ppm) or epidote from the Shamrock batholith (<4,000 ppm; Fig. 9A). Proximal epidote samples contain low mean concentrations of Sb (0.1–0.5 ppm); whereas, distal and skarn samples have slightly higher concentrations of Sb (>0.5 ppm), and Shamrock samples have

overall higher Sb values (1–5 ppm). Samples YE16AA126 (distal) and YE16AA063 (skarn) contain the widest ranges in Sb values (Fig. 9B). Antimony values for distal epidote sample YE16AA126 range between 0.1 and 500 ppm, and values for skarn epidote (YE16AA063) range between 0.001 and 300 ppm. Epidote grains from the Shamrock batholith have higher average Mn values than epidote from the Yerington batholith (Fig. 9C). Skarn epidote contains the lowest average Mn values. Arsenic values are variable in the proximal samples but decrease with distance from the center of Ann Mason. Skarn epidote also contains low As. Arsenic in epidote from the Shamrock batholith shows a range of values (0.3–20 ppm) but is higher overall than distal samples from the Yerington batholith or skarn epidote (Fig. 9D).

Cumulative average plots of LA-ICP-MS spot data

Selected trace element data from 100 LA-ICP-MS spot analyses were evaluated from sample YE16AA151 to assess the minimum number of analyses necessary to adequately represent the overall epidote composition in samples with variable chemistry. This sample was selected because it contains a single generation of epidote within a well-defined vein. Micro-XRF element maps show significant variations in epidote composition along the length of the vein (Fig. 6).

Plots of cumulative averages and relative differences to final average concentrations (n = 100) for Sr, Mn, As and Sb in epidote from sample YE16AA151 are illustrated in Figure 10. At low numbers of spot analyses ($n \leqslant 20$), the relative differences to final average values for Sr, Mn, As and Sb are greater, up to 65% relative difference (RD), than at higher numbers of spot ($n > 20$; Fig. 10). Above 40 spot analyses, the cumulative average concentrations of these elements approach the final average values (Fig. 10; < 20% RD).

Discussion

Microscale variations in epidote composition and morphology

Grainsize variations in epidote veins: A schematic diagram summarizing the primary sources of compositional variability in single generation epidote grains from the Yerington district is illustrated in Figure 11. High-resolution quantitative micro-XRF maps of epidote vein samples highlight the grain size increase and compositional changes from the vein wall to the center (Figs. 6A–I and 11). Epidote crystals grew symmetrically inward from the vein walls, with initial seed crystals increasing in size in the direction of growth (Fig. 11). Epidote grains are coarsest in the vein center, where precipitation into open space is most likely (Fig. 11). However, chemical and textural heterogeneity are not evident in all vein samples. Epidote veinlets from sample YE16AA097 (Fig. 6J–L) have a relatively homogeneous trace element distribution at the scale of imaging, both from vein edge to vein center, and also along the length of the vein.

The absence of visible trace element variation in YE16AA097 may be a limitation of the resolution of micro-XRF imaging (1 μm), or there may be a critical width necessary to generate the type of chemical variations observed in samples with wider veins (Fig. 6). Based on our observations, we favor the former explanation, given that with every step-increase in resolution, further textural and chemical complexity has been recognized. At hand sample scale, the major element compositions (e.g., epidote, clinozoisite, or piemontite) and texture of samples appear homogeneous. Visible grain-scale chemical heterogeneity is, however, detectable with SEM backscatter imaging (micron scale in this study). Textural and chemical variation are even more apparent in LA-ICP-MS element maps (4 μm pixel size), and micro-XRF images (1 μm pixel size). Nanometer pixel-size imaging of epidote-filled micro fractures and veinlets in YE16AA097 could therefore show similar, or even more complicated patterns to those discussed in this study.

Vein vs replacement epidote: Vein epidote has an order of magnitude higher As content, and 1–2 wt % lower Fe than the nearby replacement epidote grains (Figs. 6J–K). Previous studies have shown that host rock composition can be inherited by epidote, particularly the Fe-content (Holdaway, 1972; Bevins and Merriman, 1988; Grapes and Hoskin, 2004). Vein-hosted minerals are likely to have compositions dominated by the hydrothermal fluid; whereas, replacement epidote may inherit components from the altered rock. The complete replacement of primary minerals by epidote and chlorite in the wall rocks is probably a relatively slow process compared to vein infill. In mineral replacement reactions, fluids infiltrate primary minerals initially along

400 microfractures and/or grain boundaries (Jonas et al., 2013; 2014). This initial infiltration is
401 inferred to be a relatively fast process because fluids can progress large distances over short
402 periods of time, without developing reaction fronts perpendicular to grain boundaries (Ruiz-
403 Agudo et al. 2014). Progressive replacement of primary minerals in the directions perpendicular
404 to grain boundaries or microfractures can take longer, because fluids are forced to create their
405 own porosity, typically through dissolution and precipitation reactions (Ruiz-Agudo et al., 2014).
406 This slower process may favor some chemical exchange between the fluid and local minerals that
407 are recorded in the replacement epidote compositions.
408
409 *Dissolution–reprecipitation reactions*
410
411 Dissolution and reprecipitation reactions can result in crystal textures similar to those observed
412 in type 1 and type 2 epidote (Fig. 4). Kasioptas et al. (2008) demonstrated that coarse-grained
413 mineral phases can partially recrystallize to finer grained phases of the same, or related mineral
414 species. The overall morphology of grains can be maintained, but the composition can change
415 markedly (Kasioptas et al., 2008). The rate at which these reactions occur is largely a function of
416 the reactivity of the fluid (Kasioptas et al., 2008, Perdikouri et al., 2008). Putnis (2002)
417 demonstrated that when the dissolution rate is faster than the precipitation rate, there is an overall
418 volume loss that can generate pore space. In epidote samples from this study, pore space may
419 have been generated by dissolution-precipitation reactions whereby type 1 epidote was replaced
420 by fine-grained aggregates of polycrystalline epidote ± titanite and newly developed open space.
421 Type 2 epidote has overall lower Fe, and more variable Sr and Mn than type 1, which may also
422 be a function of volume change during type 2 epidote growth (Figs. 7 and 8). The presence of type
423 2 epidote around type 1 in some samples (e.g., YE16AA063; Fig. 8) indicates that type 2 epidote
424 formed after type 1.
425
426 *Chemical zoning in epidote grains*
427
428 Iron–Al zonation in both type 1 and type 2 epidote were patchy, or lamellar (Fig. 4). This type of
429 lamellar zoning, whereby the concentrations of Fe and Al typically vary between growth zones,
430 is common in epidote and can relate to growth rate and/or diffusion rates, or changes in fluid

compositions during crystal growth (i.e., oxidation state, pH; Enami et al., 2004; Grapes and Hoskin, 2004). Significant variations in Fe contents were observed in type 2 epidote (Fig. 4); however, due to its fine-grained nature, it is unclear whether individual type 2 grains have the same patchy or lamellar zoning as type 1 epidote. Each aggregate of type 2 epidote consists of hundreds of individual crystals. Variations in Fe-contents across aggregates of type 2 epidote could be due to a number of factors, including: (1) each crystal having a different Fe–Al content; (2) each crystal being zoned from rim to core; (3) lamellar zoning of individual crystals; or (4) subtle alteration of some grains.

Another factor to consider when assessing variability in epidote mineral chemistry of individual crystals is sector zoning; the process by which elements are concentrated preferentially into different crystal faces. Sector zones have been previously documented in epidote and zoisite (Dowty, 1976; Enami, 1977; Enami et al., 2004). Enami et al. (2004) noted that Fe concentration in zoisite was highest on the [101] crystal face, as compared to the [010] and [001] faces (Dollase, 1969; Frei et al., 2004; Armbruster et al., 2006). The preferential incorporation of Fe into one face over another probably occurs due to differing growth rates. [100] is the slowest growth direction and concentrates Fe (Enami et al., 2004). Sector zones in Yerington epidote were observed only in type 1 epidote (e.g. Fig. 7A–C). It may be that type 2 epidote is also sector zoned but the grainsize prevents confirmation of this hypothesis.

Exploration implications

Representative sampling of epidote: The compositional variations in epidote grains detected in the current study raise the question of statistical representation, i.e., whether the range in trace element concentrations from spot analyses in a sample sufficiently represents the overall composition of a sample. Adequate representation of maximum values can be of particular importance in resource exploration. Cooke et al. (2014a) identified that high concentrations of metals in epidote may be indicative of productive magmatic-hydrothermal systems. In the current study, between 17 and 25 spot analyses were collected from each epidote sample (Appendix B). These numbers are higher overall than the number of analyses collected per sample by Cooke et al. (2014a) at Baguio (n = 2–29; $n_{average}$ = 10). A major difference between epidote from

these districts is that Yerington epidote showed significant compositional zoning; whereas, Baguio epidote had relatively uniform major and trace element compositions (Cooke et al., 2014a).

To evaluate the optimal number of spot analyses to collect from texturally and compositionally heterogeneous epidote samples such as those detected at Yerington, we analyzed 100 spots from a single epidote vein (Fig. 10). At total spot numbers greater than 80, there is minimal difference between cumulative average values at a given number of spot analyses and the final average concentrations of Sr, Mn, As and Sb at 100 analyses (<5% RD; Fig. 10). At total spot numbers greater than 40, the RD values for Sr and Mn are low (<5% and those of As and Sb are more variable (up to 20% RD). Differences in RD values between elements at the same number of spot analyses are most likely related to the overall concentrations of each element in epidote. Elements that occur in low concentrations in epidote (<100 ppm) such as As and Sb may be more affected by outlier values in a single analysis than elements that occur in higher concentrations in epidote such as Sr and Mn. At values of $n \leqslant 40$, the average concentrations of Mn, As and Sb are consistently $\geqslant 20\%$. Therefore, to circumvent the compositional variability present in some epidotes, a higher number of spot analyses can be collected from each sample in order to ensure that the full range in element concentrations is represented by the spot data. Based on the results from Yerington, this number is around 40.

Awareness of sampling bias: To avoid contamination of LA-ICP-MS spectra by other minerals, only the most homogeneous areas of an epidote vein or epidote-altered zone of sample are typically analyzed. In sample YE16AA112, fine-grained epidote crystals in a vein occur in clustered aggregates with other minerals like albite, chlorite, and titanite (Fig. 6G–I). Sampling these areas would typically be avoided to prevent contamination of the analysis with other minerals. However, by preferentially choosing coarse-grained crystals, the user may be creating a bias in the results toward one generation of epidote formation (not necessarily the generation associated with mineralization), and or at a minimum oversampling one trace element population of epidote. Figures 8 provides another example of this potential sampling bias, whereby the most visibly homogeneous material is the coarse-grained epidote (type 1). Analyzing the fine-grained material at the nominated spot size of 30 μm results in the risk of ablating inclusions in addition

to the best epidote. The use of smaller spot sizes is not typically favored due to associated decreases in analytical precision.

Method comparison

Results from LA-ICP-MS spot data, LA-ICP-MS raster maps, and micro-XRF element maps all showed micron-scale compositional heterogeneity in epidote within a single sample (Figs. 5–9). Normal score probability plots comparing the Fe, Sr, and Mn content of two samples using the three quantitative methods applied in this study (LA-ICP-MS spots, LA-ICP-MS raster maps, and micro-XRF maps) are presented in Figure 12. In the context of this study, probability plots were used to compare element concentration data between datasets collected by different methods.

The LA-ICP-MS raster map and micro-XRF map data have similar data ranges (Fig. 12). For example, maximum values for Sr, Mn, and Fe analyzed by both methods in samples YE16AA112 are within 5% of one another (Fig. 12). Minimum values for Mn in both samples converge near 0.1 ppm (detection limit; Figs. 12B and E). Concentration differences between methods that do exist are likely a function of the location selected for analysis by each method. The locations of spot and map pixel data analyzed are different but occur within the same sample. As such, the relative amount of different epidote types (type 1 and type 2), the degree of sector zoning, and/or the amount of twinning in samples between datasets is likely to be different.

For all elements, the concentration ranges in LA-ICP-MS spot data are less than either the ranges of the LA-ICP-MS raster maps or micro-XRF maps (Fig. 12). This is due to the number of data points and the volume of material sampled in each dataset. LA-ICP-MS spot data samples a volume of ~1800 μm^3 (30 μm spot size, 2 μm depth crater). This volume is far greater than the volume of material analyzed by either the LA-ICP-MS raster map (~16 μm^3; 4 μm spot size, 1 μm depth crater) or the micro-XRF element maps (<1 μm beam width). Because the LA-ICP-MS spots homogenize a larger volume of material; the maximum and minimum values sampled by the other higher resolution methods are lost. Unlike the spots, map datasets have captured micron-size changes in Fe, Sr, and Mn content that could not be resolved with a 30 μm spot size.

One of main limitations of using synchrotron radiation for element mapping, apart from the cost of data acquisition and limited access to equipment, is the restricted list of elements that can be analyzed. With the experimental conditions used in this study, modeled after Fisher et al. (2015), the element list was restricted to those elements with K-emissions (Ca to Zr) and L-emissions (Au, Pb, Hg, W, Bi, U). This limitation is largely due to peak interferences, the atomic mass of the element and the energy of fluorescence (Ryan et al. 2014; Hare et al., 2016). Conversely, given sufficient dwell times, LA-ICP-MS raster maps can quantify most elements at the ppm level.

Conclusions

Epidote trace element compositions are currently being analyzed as part of exploration programs for porphyry Cu deposits (e.g., Cooke et al., 2017; Agnew, 2017; Agnew, 2018; Baker et al., this volume; Pacey et al., this volume). High-resolution micro-XRF and LA-ICP-MS quantitative imaging of epidote from the Yerington porphyry Cu district in Nevada has highlighted significant chemical variations at the micron-scale within single crystals of both vein and replacement epidote. Grains of vein epidote have compositions that vary significantly from the vein wall to the vein center, with up to an order of magnitude variations in As, Mn, and Sr contents, and up to 3 wt % Fe (Figs. 6 and 10). Sector zones in replacement-style epidote grains have higher concentrations of Fe, Mn, Sr, As, Sb, and Ce than other crystal faces (Figs. 7A–C, 8). Furthermore, subtle compositional differences were detected between replacement epidote and vein epidote in the same sample (Fig. 6J–L). Vein epidote had nearly an order of magnitude more As than replacement epidote.

We suggest that in prospective exploration areas where epidotes are characterized by crystallographic features such as sector zones or twins, detailed high-resolution microscopy is undertaken to characterize textures and paragenetic relationships of the mineral phases of interest. Alternatively, as demonstrated in the current study, more laser spot analyses can be collected (~$n > 40$) to ensure a statistically robust dataset that records the full range of compositional data. Where possible, an effort should be made to analyze and compare consistent epidote sample types (vein or replacement) and similar areas within those sample types (vein wall vs. vein center) to ensure the best comparison possible between laser spot data points.

Acknowledgements

This research is part of a PhD study funded by the AMIRA International P1153 project 'Applying the explorer's toolbox to discover Cu, Au, and Mo deposits', an Australian post-graduate award, and an AusIMM Education Endowment Fund scholarship. Analytical work was undertaken on the X-ray fluorescence microscopy beamline at the Australian Synchrotron, part of ANSTO. We acknowledge travel funding and accommodation provided by the Australian Synchrotron. Sincere thanks to Mason Resources (formerly Entrée Gold), Mason Valley Copper, and Quaterra Resources for access to leases for sample collection purposes. A particular thanks to John Dilles, Dick Tosdal, Josh Phillips, Amos Garay, Matt Cunningham, Hank Ohlin, and George Eliopolous for assistance in the field. Thanks to Al Cuison at the University of Tasmania lapidary for sample preparation, and to Sandrin Feig and Karsten Goemann for assistance using SEM facilities at the University of Tasmania. We thank Matthew Cracknell for help using the software KNIME. This manuscript benefited greatly from discussions with Shawn Hood, Michael Baker, Paul Olin and Evan Orovan, as well as thorough reviews by Irene del Real Contreras and an anonymous reviewer.

References

Agnew, P.I., 2017, Geochemistry – State of the Art 2017, Exploration 17 conference abstract, Toronto, Canada, 2017, 1p.

Alva-Jimenez, T., Tosdal, R.M., Dipple, G., Dilles, J.H., Kent, A.J.R., and Halley, S., this volume, Chemical variations in hydrothermal muscovite across the Highland Valley porphyry Cu-Mo district, British Columbia, Canada: Economic Geology, this volume.

Armbruster, T., Bonazzi, P., Akasaka, M., Bermanec, V., Chopin, C., Gieré, R., Heuss–Assbichler, S., Liebscher, A., Menchetti, S., and Yuanming, P., 2006, Recommended nomenclature of epidote–group minerals: European Journal of Mineralogy, v. 18, p. 551–567.

Baker, M.J., Wilkinson, J.J., Wilkinson, C.C., Cooke, D.R. and Ireland, T.J., this volume, Epidote trace element chemistry as an exploration tool: a case study from the Collahuasi district, northern Chile: Economic Geology, this volume.

585 Ballard, J.R., Palin, M.J., and Campbell, I.H., 2002, Relative oxidation states of magmas inferred
586 from Ce (IV)/Ce (III) in zircon: Application to porphyry copper deposits of northern Chile:
587 Contributions to Mineralogy and Petrology, v. 144, p. 347–364.

588 Bevins, R., and Merriman, R., 1988, Compositional controls on coexisting prehnite-actinolite and
589 prehnite-pumpellyite facies assemblages in the Tal y Fan metabasite intrusion, North Wales:
590 Implications for Caledonian metamorphic field gradients: Journal of Metamorphic Geology,
591 v. 6, p. 17–39.

592 Byrne, K., Lesage, G., Gleeson, S., and Lee, R., 2016, Large-scale sodic–calcic alteration around
593 porphyry popper pystems: Examples from the Highland Valley Copper District, Guichon
594 Batholith, South-Central British Columbia: Geoscience BC Summary of Activities, p. 2017–
595 1.

596 Carten, R.B., 1986, Sodium-calcium metasomatism; chemical, temporal, and spatial relationships
597 at the Yerington, Nevada, porphyry copper deposit: Economic Geology, v. 81, p. 1495–1519.

598 Chang, Z., Hedenquist, J.W., White, N.C., Cooke, D.R., Roach, M., Deyell, C L., Garcia, J.,
599 Gemmell, J. B., McKnight, S., and Cuison, A.L., 2011, Exploration tools for linked porphyry
600 and epithermal deposits: Example from the Mankayan intrusion-centered Cu-Au district,
601 Luzon, 1)Philippines: Economic Geology, v. 106, p. 1365–1398.

602 Chukanov, N.V., Varlamov, D.A., Nestola, F., Belakovskiy, D.I., Goettlicher, J., Britvin, S.N.,
603 Lanza, A., and Jancev, S., 2012, Piemontite-(Pb), CaPbAl2Mn3+[Si2O7][SiO4]O(OH), a new
604 mineral species of the epidote supergroup: Journal of Mineralogy and Geochemistry, v. 189,
605 p. 275–286.

606 Cooke, D.R., Wilkinson, J.J., Baker, M.J., Agnew, P., Phillips, J., Martin, H., Chang, Z., Hollings,
607 P., Chen, H., Wilkinson, C.C., Inglis, S.J. Gemmell, J.B., Danyushevsky, L., and Gilbert, S.,
608 this volume, Using mineral chemistry to aid exploration – a case study from the Resolution
609 porphyry Cu-Mo deposit, Arizona: Economic Geology, this volume.

610 Cooke, D.R., Hollings, P., and Walshe, J.L., 2005, Giant porphyry deposits: characteristics,
611 distribution, and tectonic controls: Economic Geology, v. 100, p. 801–818.

612 Cooke, D.R., Baker, M., Hollings, P., Sweet, G., Chang, Z., Danyushevsky, L., Gilbert, S., Zhou, T.,
613 White, N.C., and Gemmell, J.B., 2014a, New advances in detecting the distal geochemical

614 footprints of porphyry pystems—Epidote mineral chemistry as a tool for vectoring and
615 fertility assessments, Society of Economic Geologists Special Publication, v. 18, p. 127–152.

616 Cooke, D., Gemmell, J., Wilkinson, J., Hollings, P., Baker, M., Zhang, L., Fox, N., White, N., Chen,
617 H., and Pacey, A., 2014b, Executive summary AMIRA project P1060: enhanced geochemical
618 targeting in magmatic-hydrothermal systems, AMIRA, Hobart, Tasmania, P1060, 2014, p.

619 Cooke, D.R., Hollings P., Wilkinson J.J., and Tosdal R.M., 2014c, Geochemistry of porphyry
620 deposits: Treatise on Geochemistry, 2nd ed., v. 13, p. 357−381.

621 Cooke, D.R. and Agnew, P., Hollings, P., Baker, M., Chang, Z., Wilkinson, J.J., White, N.C. Zhang,
622 L., Thompson, J., Gemmell, J.B., Fox, N., Chen, H., and Wilkinson, C.C., 2017, Porphyry
623 indicator minerals (PIMS) and porphyry vectoring and fertility tools (PVFTS) – Indicators
624 of mineralization styles and recorders of hypogene geochemical dispersion halos,
625 Proceedings of Exploration 17: Sixth Decennial International Conference on Mineral
626 Exploration, 22-25 October 2017, Toronto, Ontario, pp. 457−470.

627 De Boer, D., Borstrok, J., Leenaers, A., Van Sprang, H., and Brouwer, P., 1993, How accurate is
628 the fundamental parameter approach? XRF analysis of bulk and multilayer samples: X-Ray
629 Spectrometry, v. 22, p. 33–38.

630 Dilles, J.H., 1984, The petrology and geochemistry of the Yerington batholith and the Ann-Mason
631 porphyry copper deposit, Western Nevada: Unpublished Ph.D. thesis, Palo Alto, USA,
632 Stanford University, 522 p.

633 Dilles, J.H., 1987, Petrology of the Yerington Batholith, Nevada: Evidence for evolution of
634 porphyry copper ore fluids: Economic Geology, v. 82, p. 1750–1789.

635 Dilles, J.H., and Wright, J.E., 1988, The chronology of early Mesozoic arc magmatism in the
636 Yerington district of western Nevada and its regional implications: Geological Society of
637 America Bulletin, v. 100, p. 644–652.

638 Dilles, J.H., and Einaudi, M.T., 1992, Wall-rock alteration and hydrothermal flow paths about the
639 Ann-Mason porphyry copper deposit, Nevada: A 6–km vertical reconstruction: Economic
640 Geology, v. 87, p. 1963–2001.

641 Dilles, J.H., Solomon, G.C., Taylor, H.P., and Einaudi, M.T., 1992, Oxygen and hydrogen isotope
642 characteristics of hydrothermal alteration at the Ann-Mason porphyry copper deposit,
643 Yerington, Nevada: Economic Geology, v. 87, p. 44–63.

644 Dilles, J.H., Kent, A.J., Wooden, J.L., Tosdal, R.M., Koleszar, A., Lee, R.G., and Farmer, L.P., 2015,
645 Zircon compositional evidence for sulfur-degassing from ore-forming arc magmas:
646 Economic Geology, v. 110, p. 241–251.

647 Dollase, W., 1969, Crystal structure and cation ordering of piemontite: American Mineralogist, v.
648 54, p. 710–717.

649 Dowty, E., 1976, Crystal structure and crystal growth: Sector zoning in minerals: American
650 Mineralogist, v. 61, p. 460–469.

651 Einaudi, M.T., 1977, Petrogenesis of the copper-bearing skarn at the Mason Valley Mine,
652 Yerington District, Nevada: Economic Geology, v. 72, p. 769–795.

653 Einaudi, M.T., 1982, Description of skarns associated with porphyry copper plutons,
654 southwestern North America: Advances in geology of the porphyry copper deposits,
655 Southwestern North America: University of Arizona Press, Tucson, Arizona, p. 139–184.

656 Enami, M., 1977, Sector zoning of zoisite from a metagabbro at Fujiwara, Sanbagawa
657 metamorphic terrain in central Shikoku: Journal of the Geological Society of Japan, v. 83, p.
658 693–697.

659 Enami, M., Liou, J., and Mattinson, C., 2004, Epidote minerals in high P/T metamorphic terranes:
660 Subduction zone and high–to ultrahigh–pressure metamorphism: Reviews in Mineralogy
661 and Geochemistry, v. 56, p. 347–398.

662 Fisher, L.A., Fougerouse, D., Cleverley, J.S., Ryan, C.G., Micklethwaite, S., Halfpenny, A., Hough,
663 R. M., Gee, M., Paterson, D., and Howard, D.L., 2015, Quantified, multi-scale X-ray
664 fluorescence element mapping using the Maia detector array: Application to mineral
665 deposit studies: Mineralium Deposita, v. 50, p. 665–674.

666 Frei, D., Liebscher, A., Franz, G., and Dulski, P., 2004, Trace element geochemistry of epidote
667 minerals: Reviews in Mineralogy and Geochemistry, v. 56, p. 553–605.

668 Grapes, R.H., and Hoskin, P.W., 2004, Epidote group minerals in low-medium pressure
669 metamorphic terranes: Reviews in Mineralogy and Geochemistry, v. 56, p. 301–345.

670 Gustafson, L.B., and Hunt, J.P., 1975, The porphyry copper deposit at El Salvador, Chile:
671 Economic Geology, v. 70, p. 857–912.

672 Hare, D.J., Jones, M.W., Wimmer, V.C., Jenkins, N.L., de Jonge, M.D., Bush, A.I., and McColl, G.,
673 2016, High-resolution complementary chemical imaging of bio-elements in Caenorhabditis
674 elegans: Metallomics, v. 8, p. 156–160.

675 Harris, N.B., and Einaudi, M.T., 1982, Skarn deposits in the Yerington District, Nevada;
676 metasomatic skarn evolution near Ludwig: Economic Geology, v. 77, p. 877–898.

677 Holdaway, M., 1972, Thermal stability of Al–Fe epidote as a function of Fe content: Contributions
678 to Mineralogy and Petrology, v. 37, p. 307–340.

679 Jonas, L., John, T., and Putnis, A., 2013, Influence of temperature and Cl on the hydrothermal
680 replacement of calcite by apatite and the development of porous microstructures: American
681 Mineralogist, v. 98, p. 1516–1525.

682 Jonas, L., John, T., King, H.E., Geisler, T., and Putnis, A., 2014, The role of grain boundaries and
683 transient porosity in rocks as fluid pathwyas for reaction front propagation: Earth and
684 Planetary Science Letters, v. 386, 64–74.

685 Kasioptas, A., Perdikouri, C., Putnis, C., and Putnis, A., 2008, Pseudomorphic replacement of
686 single calcium carbonate crystals by polycrystalline apatite: Mineralogical Magazine, v. 72,
687 p. 77–80.

688 Kolitsch, U., Mills, S.J., Miyawaki, R., and Blass, G., 2012, Ferriallanite-(La), a new member of the
689 epidote supergroup from the Eifel, Germany: European Journal of Mineralogy, v. 24, p. 741–
690 747.

691 Kulla, G., Oshust, P., Desautels, J.R.P., Melnyk, J., Zurowski, G., Jones, L., and Colantonio, M.,
692 2015, Updated preliminary economic assessment on the Ann Mason project Nevada, U.S.A,
693 AMEC Foster Wheeler Americas Ltd., 361p.

694 Large, R.R., Danyushevsky, L., Hollit, C., Maslennikov, V., Meffre, S., Gilbert, S., Bull, S., Scott,
695 R., Emsbo, P., and Thomas, H., 2009, Gold and trace element zonation in pyrite using a laser
696 imaging technique: implications for the timing of gold in orogenic and Carlin-style
697 sediment-hosted deposits: Economic Geology, v. 104, p. 635–668.

698 Lee, R.G., Dilles, J.H., Tosdal, R.M., Wooden, J.L., and Mazdab, F.K., 2017, Magmatic evolution of
699 granodiorite intrusions at the El Salvador porphyry copper deposit, Chile, based on trace
700 element composition and U/Pb age of zircons: Economic Geology, v. 112, p. 245–273.

Longerich, H.P., Jackson, S.E., and Günther, D., 1996, Inter-laboratory note. Laser ablation inductively coupled plasma mass spectrometric transient signal data acquisition and analyte concentration calculation: Journal of Analytical Atomic Spectrometry, v. 11, p. 899–904.

Lowell, J.D., and Guilbert, J.M., 1970, Lateral and vertical alteration-mineralization zoning in porphyry ore deposits: Economic Geology, v. 65, p. 373–408.

Lu, Y.-J., Loucks, R.R., Fiorentini, M., McCuaig, T. C., Evans, N. J., Yang, Z.-M., Hou, Z.-Q., Kirkland, C. L., Parra-Avila, L. A., and Kobussen, A., 2016, Zircon compositions as a pathfinder for porphyry Cu±Mo±Au deposits: Economic Geology Special Publication, v. 19, p. 329–347.Pacey, A., 2016, The characteristics, geochemistry and origin of propylitic alteration in the Northparkes porphyry Cu-Au system: Unpublished Ph.D. thesis, Imperial College London, London, 652 p.

Pacey, A., Wilkinson, J.J., and Cooke, D.R., this volume; Chlorite and epidote mineral chemistry in porphyry ore systems: A case study of the Northparkes district, NSW, Australia: Economic Geology, this volume.

Paterson, D., De Jonge, M., Howard, D., Lewis, W., McKinlay, J., Starritt, A., Kusel, M., Ryan, C., Kirkham, R., and Moorhead, G., 2011, The X-ray Fluorescence Microscopy Beamline at the Australian Synchrotron: AIP Conference Proceedings, 2011, p. 219−222.

Perdikouri, C., Kasioptas, A., Putnis, C., and Putnis, A., 2008, The effect of fluid composition on the mechanism of the aragonite to calcite transition: Mineralogical Magazine, v. 72, p. 111–114.

Proffett, J.M., 1977, Cenozoic geology of the Yerington district, Nevada, and implications for the nature and origin of Basin and Range faulting: Geological Society of America Bulletin, v. 88, p. 247–266.

Proffett, J.M., and Dilles, J.H., 1984, Geologic map of the Yerington district, Nevada, Nevada Bureau of Mines and Geology Map 77.

Putnis, A., 2002, Mineral replacement reactions: from macroscopic observations to microscopic mechanisms: Mineralogical Magazine, v. 66, p. 689–708.

Ryan, C., 2000, Quantitative trace element imaging using PIXE and the nuclear microprobe: International Journal of Imaging Systems and Technology, v. 11, p. 219–230.

731 Ruiz-Agudo, E., Putnis, C., and Putnis, A., 2014, Coupled dissolution and precipitation at
732 mineral-fluid interfaces: Chemical Geology, v. 383, p. 132–146.

733 Ryan, C., 2000, Quantitative trace element imaging using PIXE and the nuclear microprobe:
734 International Journal of Imaging Systems and Technology, v. 11, p. 219–230.

735 Ryan, C., Etschmann, B., Vogt, S., Maser, J., Harland, C., Van Achterbergh, E., and Legnini, D.,
736 2005, Nuclear microprobe–synchrotron synergy: Towards integrated quantitative real-time
737 elemental imaging using PIXE and SXRF: Nuclear Instruments and Methods in Physics
738 Research Section B: Beam Interactions with Materials and Atoms, v. 231, p. 183–188.

739 Ryan, C., Kirkham, R., Hough, R., Moorhead, G., Siddons, D., De Jonge, M., Paterson, D., De
740 Geronimo, G., Howard, D., and Cleverley, J., 2010a, Elemental X–ray imaging using the
741 Maia detector array: The benefits and challenges of large solid-angle: Nuclear Instruments
742 and Methods in Physics Research Section A: Accelerators, Spectrometers, Detectors and
743 Associated Equipment, v. 619, p. 37–43.

744 Ryan, C., Siddons, D., Kirkham, R., Dunn, P., Kuczewski, A., Moorhead, G., De Geronimo, G.,
745 Paterson, D., De Jonge, M., and Hough, R., 2010b, The new Maia detector system: methods
746 for high definition trace element imaging of natural material: AIP Conference Proceedings,
747 2010b, p. 9–17.

748 Ryan, C.G., Siddons, D.P., Kirkham, R.; Li, Z.Y.; de Jonge, M.D., Paterson, D.J., Kuczewski, A.,
749 Howard, D.L., Dunn, P.A., Falkenberg, G., Boesenberg, U., De Geronimo, G., Fisher, L.A.,
750 Halfpenny, A., Lintern, M.J., Lombi, E., Dyl, K.A., Jensen, M., Moorhead, G.F., Cleverley,
751 J.S., Hough, R.M., Godel, B., Barnes, S.J., James, S.A., Spiers, K.M., Alfeld, M., Wellenreuther,
752 G., Vukmanovic, Z., Borg, S.: Journal of Physics Conference Series, 22nd International
753 Congress on X-Ray Optics and Microanalysis, 2014, v. 499, 13 p.

754 Uribe-Mogollon, C., and Maher, K., 2018, White mica geochemistry of the Copper Cliff porphyry
755 Cu deposit: Insights from a vectoring tool applied to exploration: Economic Geology v. 113,
756 p. 1269–1295.

757 Wilkinson, J.J., Chang, Z., Cooke, D.R., Baker, M. J., Wilkinson, C.C., Inglis, S., Chen, H., and
758 Gemmell, J.B., 2015, The chlorite proximitor: A new tool for detecting porphyry ore deposits:
759 Journal of Geochemical Exploration, v. 152, p. 10–26.

760 Wilkinson, J.J., Baker, M., Cooke, D.R., Wilkinson, C.C., and Inglis, S., 2017, Exploration targeting
761 in porphyry Cu systems using propylitic mineral chemistry: A case study of the El Teniente
762 deposit, Chile [Ext. Abs.]: SGA Biennial Meeting, 14th, Quebec, Canada, 2017, Conference
763 Proceedings, 4 p.

764 Wilkinson, J.J., Baker, M.J., Cooke, D.R. and Wilkinson, C.C., this volume, Exploration targeting
765 in porphyry Cu systems using propylitic mineral chemistry: A case study of the El Teniente
766 deposit, Chile: Economic Geology, this volume.
767

Table 1. Sample descriptions. UTM coordinates are provided in in NAD83 Zone11. Mineral abbreviations: Act = actinolite; Alb = albite; Chl = chlorite; Di = diopside; Ep = epidote; and Py = pyrite.

Sample	YE16AA001	YE16AA063	YE16AA097	YE16AA112	YE16AA126	YE16AA151	YE16AA212
Easting	306684	303185	306232	305023	305311	304761	304155
Northing	4314832	4312925	4312966	4313378	4315236	4317202	4317442
RL	1627	1587	1688	1913	1876	1706	1064
Sample description							
Rock unit	McLeod Hill quartz monzodiorite	Shamrock monzonite	Shamrock monzonite	Shamrock monzonite	McLeod Hill quartz monzodiorite	McLeod Hill quartz monzodiorite	McLeod Hill quartz monzodiorite
Visible alteration	Ep–alb–act–ttn	Ep–di–alb–act–qtz	Ep–alb–act	Ep–alb–act	Ep–alb–act–chl	Ep–alb	Ep–alb–py
Vein	-	-	Ep	Ep–chl	Ep–act–alb	Ep	Qtz–py–ep
Vein width (cm)	-	-	<0.1	0.2	0.7	<0.1	0.2
Vein halo mineralogy	-	-	Ep–alb–act	Ep–alb–act	Ep–alb–act	Ep-alb–act	Ep–alb–py
Vein halo width (cm)	-	-	2–3	1–3	2–4	1–2	<1
Analysis							
SEM	Yes	Yes	Yes	Yes	Yes	Yes	Yes
LA-ICP-MS spot analysis	Yes	Yes	Yes	Yes	Yes	Yes	Yes
LA-ICP-MS map	-	Yes	-	-	-	-	-
XFM	Yes	Yes	Yes	Yes	Yes	Yes	Yes
Location classification	Distal	Skarn	Shamrock	Shamrock	Distal	Proximal	Proximal

Fig. 1: Geology map of the Ann Mason fault block, Yerington district, Nevada showing the locations of samples used in this study. Map modified from Proffett and Dilles (1984). The Ann Mason and Blue Hill porphyry Cu deposit resources (0.15% Cu grade shells projected to surface) are shown by stippled outlines (Kulla et al., 2015; Watkins et al., 2015). Skarn-Cu deposits within the Ann Mason fault block (Casting Copper and Ludwig) are shown. Major basin and range-style normal faults are shown by thicker black lines. The Ann Mason fault block is bound to the east by the Bluestone fault, and to the north by the Singatse fault. U–Pb rock ages from Dilles and Wright (1988).

Fig. 2: Hand specimen photographs of samples analyzed in this study: A. YE16AA001: Epidote–actinolite–titanite clots with albite-dominant alteration halos in McLeod Hill quartz monzodiorite. B. YE16AA063: Epidote–diopside–actinolite–albite–quartz altered Shamrock monzonite. C. YE16AA097: Epidote veinlets with albite–epidote–actinolite vein halos in Shamrock monzonite. D. YE16AA112: Epidote–chlorite vein with epidote–albite–actinolite vein halo in Shamrock monzonite. E. YE16AA126: Epidote–albite–actinolite vein in McLeod Hill quartz monzodiorite. F. YE16AA151: Epidote veinlet with albite–epidote vein halo in McLeod Hill quartz monzodiorite. G. YE16AA212: Quartz–pyrite–epidote veins in McLeod Hill quartz monzodiorite. Laser mount (25 mm diameter) locations are shown by the thick dashed white line, as labelled in Figure 2A.

Fig. 3: Large-scale SEM backscatter electron images of selected samples showing mineral associations and epidote morphology: A. YE16AA063: Coarse-grained epidote with quartz and minor actinolite. B. YE16AA112: Epidote–chlorite vein with albite and minor epidote in vein halo. C. YE16AA126: Vein-hosted epidote–albite–actinolite–titanite. D. YE16AA151: Epidote veinlet with actinolite–titanite–epidote–quartz in vein halo. Dashed red lines denote locations of high resolution XRF maps presented in Figures 6 and 7. High resolution XRF maps of YE16AA112 shown in Figure 6 are in a similar location to the entire view shown in Figure 3B.

Fig. 4: SEM backscatter electron images of epidote showing two epidote classes. Type 1 epidote (Ep1) is coarse-grained (generally >50 µm diameter crystals) and weakly zoned with respect to Fe and Al. Type 2 epidote (Ep2) occurs as fine-grained aggregates (<30 µm diameter crystals), with pits and/or inclusions of other minerals. Representative Fe concentrations, collected by energy dispersive spectra on the SEM, are shown for type 1 and type 2 epidote. A. Sample YE16AA001: Type 1 epidote surrounded by type 2. B. YE16AA063: Type 1 epidote flanked by type 2. C. YE16AA112: Intergrown type 1 and type 2 epidote with chlorite. D. YE16AA126: Type 1 epidote surrounded by type 2. E. YE16AA151: Vein with mostly type 1 epidote, and type 2 along fractures. Mineral abbreviations: Ab = albite; Chl = chlorite; Ep = epidote; Qtz = quartz; Ttn = titanite.

Fig. 5: Micro-XRF element map overview scans (6 µm pixel size) from two samples. A–F: YE16AA151 contains a thin epidote vein (<250 µm wide) with a 1–2 cm-wide epidote–albite vein halo. A. Ca, B. Fe, C. Sr, D. Mn, E. Cu, F. Zn. Calcium, Fe, Sr, and Mn are concentrated in the epidote vein. Iron, Sr, and Mn define the vein halo. Copper and Zn are concentrated in actinolite relative to epidote. G–H: YE16AA126 contains a 0.7 cm-wide irregular vein and epidote–albite vein halo, with thin (<1 mm wide) epidote veinlets oriented at 45° to the main alteration zone. G. Ca, H. RGB image of Fe, Mn, and Sr, and I. Co. J–L: YE16AA097 contains a series of epidote veinlets and patches of actinolite replaced by epidote. J. Ca, K. Sr, L. Zn. Abbreviations: Ab = albite; Act = actinolite; Chl = chlorite; Ep = epidote; Py = pyrite; Repl = replacement; Ttn = titanite. Element concentrations are based on a spectral fit to epidote, therefore concentrations of these elements in other minerals are only semi-quantitative.

Fig. 6: XRF quantitative element maps of epidote veins. A–F. Epidote vein and vein splay from sample YE16AA151. The main epidote vein can be divided into three discrete zones based on epidote composition (labeled 1–3 and shown by dashed line). Zone 1 contains low Sr and Mn, and elevated Fe. Zone 2 contains elevated Sr and As, and low Fe and Mn. Zone 3 contained low Sr, and Fe, and elevated Mn and As. Copper is below detection limit in vein epidote, but is concentrated in actinolite outside the vein. G–I: Epidote vein and vein splay from YE16AA112. Sr is concentrated in epidote, and Mn is concentrated in chlorite in the alteration. Dashed line denotes boundary between fine-grained (top) and coarse-grained vein epidote. Arsenic (6H) occurs preferentially in coarse-grained epidote located below the dashed line. 6I shows Sr in grayscale to highlight textural differences between coarse and fine-grained epidote. J–L: Vein and replacement epidote from sample YE16AA097. Vein epidote has lower Fe, and higher As compared to replacement epidote. Figures 6F and 6G are RGB element maps. Ab = albite; Act = actinolite; Chl = chlorite; Ep = epidote; Hbl = hornblende; Zr = zircon; Vn = vein; Rpl = replacement. The locations of high resolution images are included in Figures 3 and 5.

Fig. 7. Quantitative micro-XRF element maps from two samples. A–C: Sample YE16AA063. A. Sector zoned Sr in coarse-grained type 1 epidote (Ep1) with patchy Sr in type 2 epidote (Ep2). B. Fe concentrated in the cores of type 1 epidote. C. Mn is concentrated along epidote grain boundaries and in cores of type 1 epidote. D–F: Sample YE16AA126. D. RGB image Ca, Fe, Mn, E. Cu, F. Mn, and G. Sr.

Fig. 8. LA-ICP-MS element map from sample YE16AA063. An SEM backscatter image for this element map is shown in Figure 4B. A. Fe, B. Mn, C. Sr, D. As, E. Sb, and F. Ce. Element concentrations in ppm. The location of this element map is approximately 2 mm away from the location of the micro-XRF element map shown in Figure 7. The white stippled line separates type 1 epidote (Ep1) inside, from type 2 epidote (Ep2) outside the line. Type 1 epidote contains consistently elevated values of Fe, Mn, Sr, As, Sb, and Ce. Type 2 epidote contains variable concentrations of Fe, Mn, Sr, and Ce, but contains no As or Sb.

Fig. 9. A–D: Box and whisker plots of LA-ICP-MS data from samples analyzed in this study. Samples are ordered with respect to distance from the center of Ann Mason, from proximal (left) to distal (right) with a solid line separating samples from the Yerington batholith (left) from the Shamrock batholith (right). A. Sr, B. Sb, C. Mn, and D. As.

Fig. 10. Plots of cumulative average values and relative differences (RD) from final average values (n = 100) in vein sample YE16AA151 of: A. Sr, B. Mn, D. As, and E. Sb. RD values were calculated by taking the absolute difference between the final average values for a given element (at n = 100) and the cumulative average at a given number of analyses, divided by the final average value and multiplying the quotient by 100 to obtain %RD.

Fig. 11. Schematic diagram showing changes in grainsize and epidote composition from the vein margin to the vein center. Epidote close to wall rock is fine-grained and may have inherited chemical components from wall rock minerals. Epidote at the vein-center is coarser-grained and is likely to have chemistry dominated by the associated hydrothermal fluid. Coarser-grained epidote can show twins, lamellar zones and sector zones, which contribute to micron-scale geochemical variability within individual epidote crystals.

Fig. 12. Normal score probability plots comparing Sr, Mn, and Fe contents in epidote from the same samples using LA-ICP-MS spot analysis, LA-ICP-MS raster map pixel data, and micro-XRF map pixel data. A–C: YE16AA112. A. Sr, B. Mn, C. Fe. D–F: YE16AA063. D. Sr, E. Mn, and F. Fe.

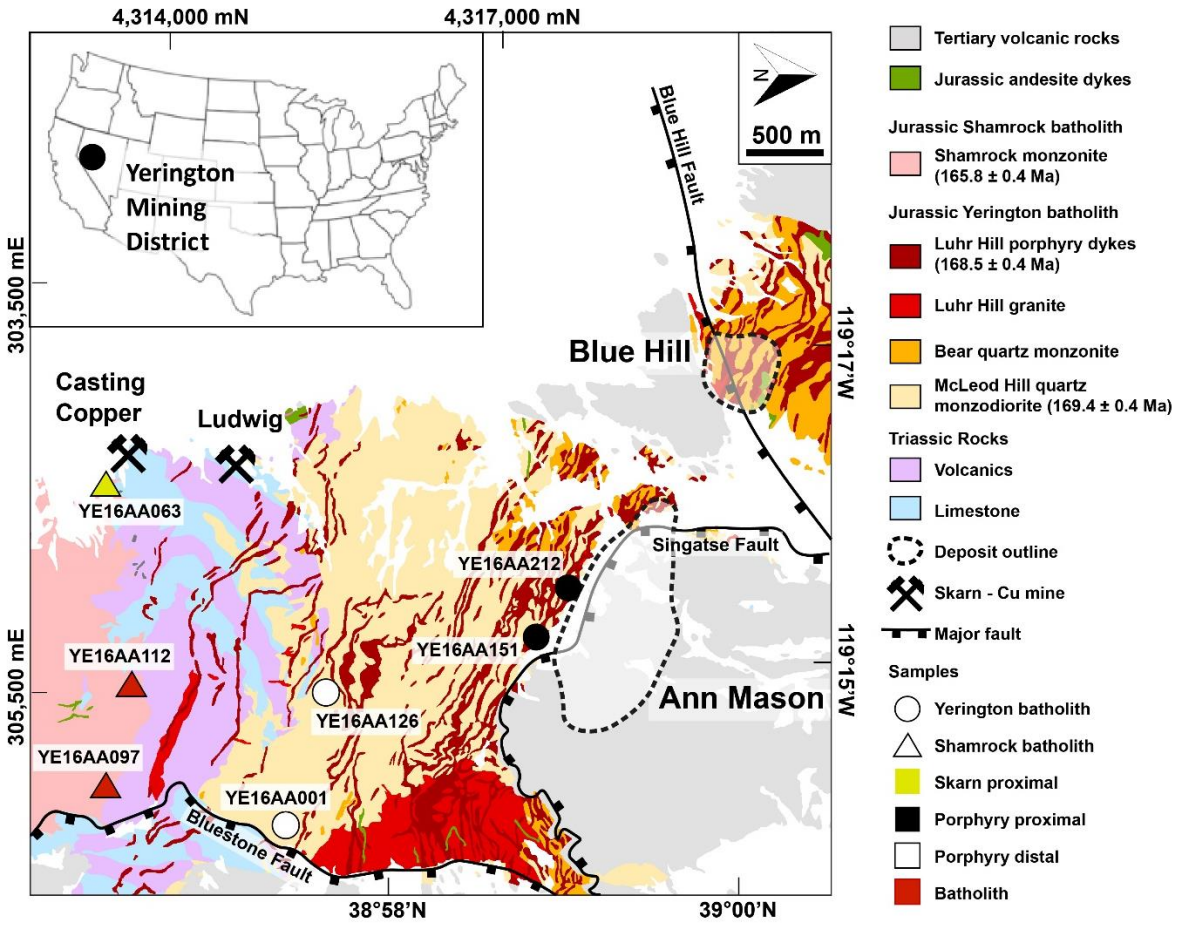
4,314,000 mN
4,317,000 mN
303,500 mE
305,500 mE
119°17'W
119°15'W
38°58'N
39°00'N
Yerington
Mining
District
N
500 m
Blue Hill Fault
Blue Hill
Casting
Copper
Ludwig
YE16AA063
YE16AA212
Singatse Fault
YE16AA112
YE16AA151
YE16AA126
Ann Mason
YE16AA097
YE16AA001
Bluestone Fault
Tertiary volcanic rocks
Jurassic andesite dykes
Jurassic Shamrock batholith
Shamrock monzonite
(165.8 ± 0.4 Ma)
Jurassic Yerington batholith
Luhr Hill porphyry dykes
(168.5 ± 0.4 Ma)
Luhr Hill granite
Bear quartz monzonite
McLeod Hill quartz
monzodiorite (169.4 ± 0.4 Ma)
Triassic Rocks
Volcanics
Limestone
Deposit outline
Skarn - Cu mine
Major fault
Samples
Yerington batholith
Shamrock batholith
Skarn proximal
Porphyry proximal
Porphyry distal
Batholith

Figure 1

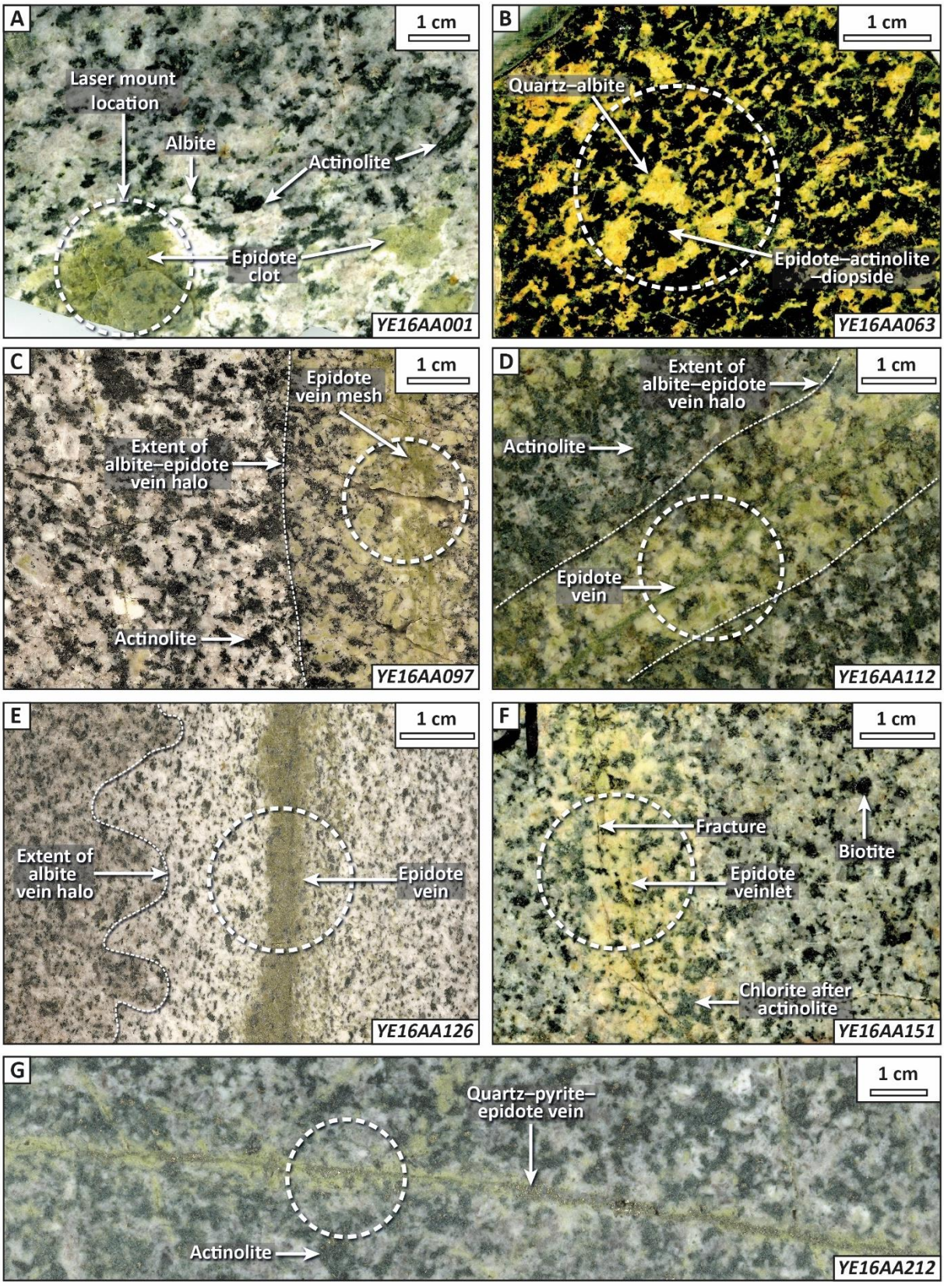
A
1 cm
Laser mount location
Albite
Actinolite
Epidote clot
YE16AA001
B
1 cm
Quartz–albite
Epidote–actinolite –diopside
YE16AA063
C
1 cm
Epidote vein mesh
Extent of albite–epidote vein halo
Actinolite
YE16AA097
D
1 cm
Extent of albite–epidote vein halo
Actinolite
Epidote vein
YE16AA112
E
1 cm
Extent of albite vein halo
Epidote vein
YE16AA126
F
1 cm
Fracture
Biotite
Epidote veinlet
Chlorite after actinolite
YE16AA151
G
1 cm
Quartz–pyrite–epidote vein
Actinolite
YE16AA212

Figure 2

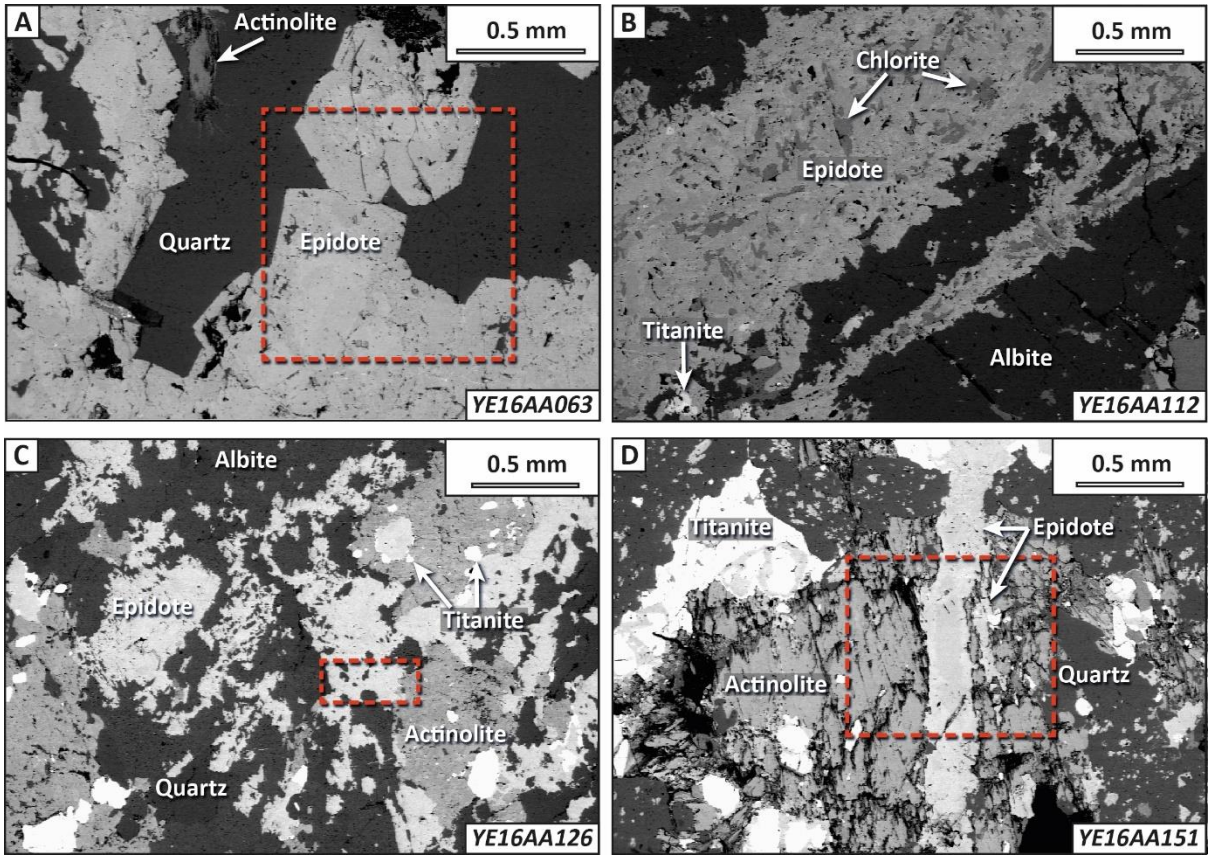
A
Actinolite
0.5 mm
Quartz
Epidote
YE16AA063
B
0.5 mm
Chlorite
Epidote
Titanite
Albite
YE16AA112
C
Albite
0.5 mm
Epidote
Titanite
Actinolite
Quartz
YE16AA126
D
0.5 mm
Titanite
Epidote
Actinolite
Quartz
YE16AA151

Figure 3

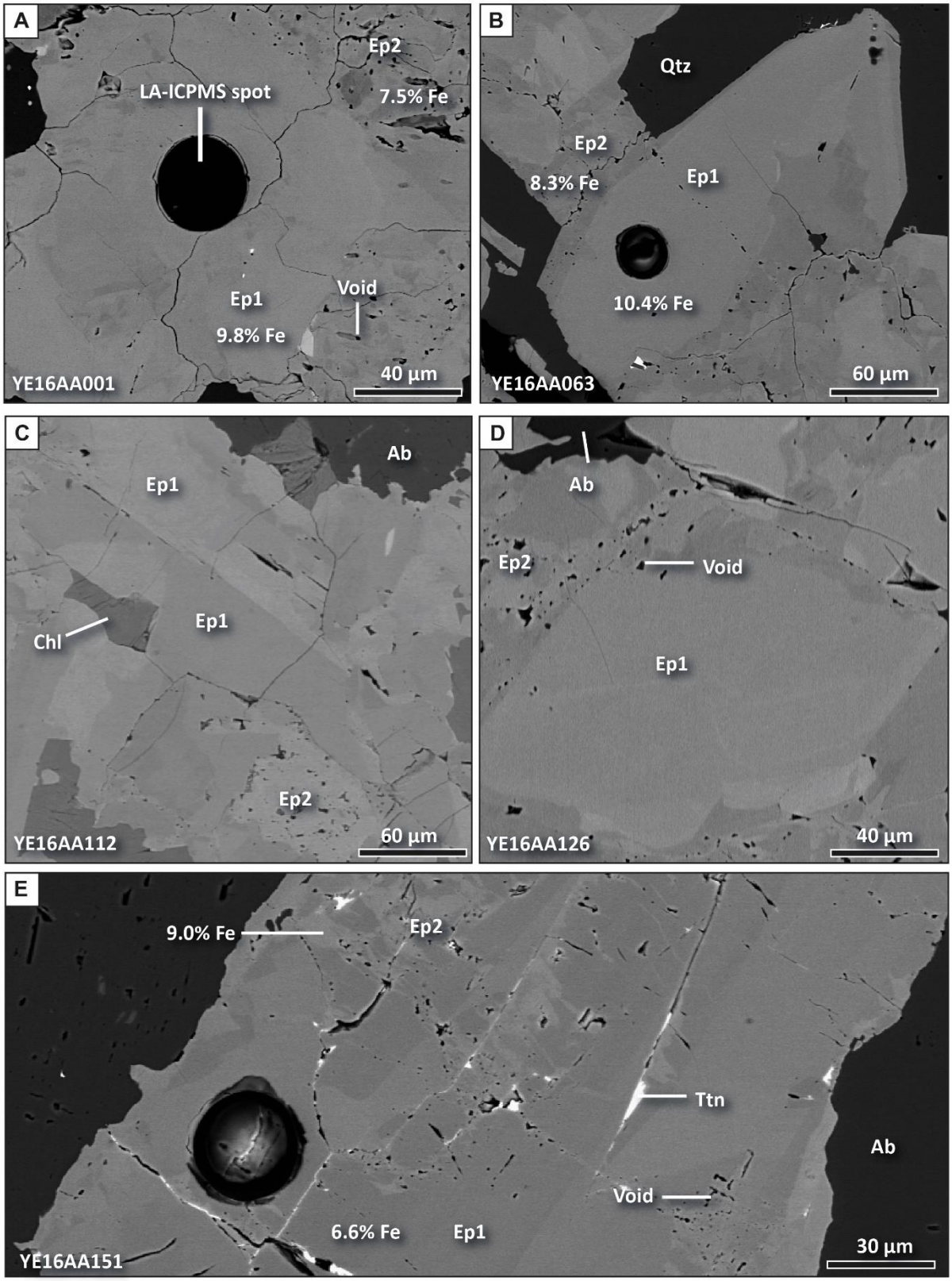
A
Ep2
LA-ICPMS spot
7.5% Fe
Ep1
Void
9.8% Fe
YE16AA001
40 µm
B
Qtz
Ep2
8.3% Fe
Ep1
10.4% Fe
YE16AA063
60 µm
C
Ab
Ep1
Ep1
Chl
Ep2
YE16AA112
60 µm
D
Ab
Ep2
Void
Ep1
YE16AA126
40 µm
E
9.0% Fe
Ep2
Ttn
Ab
Void
6.6% Fe
Ep1
YE16AA151
30 µm

Figure 4

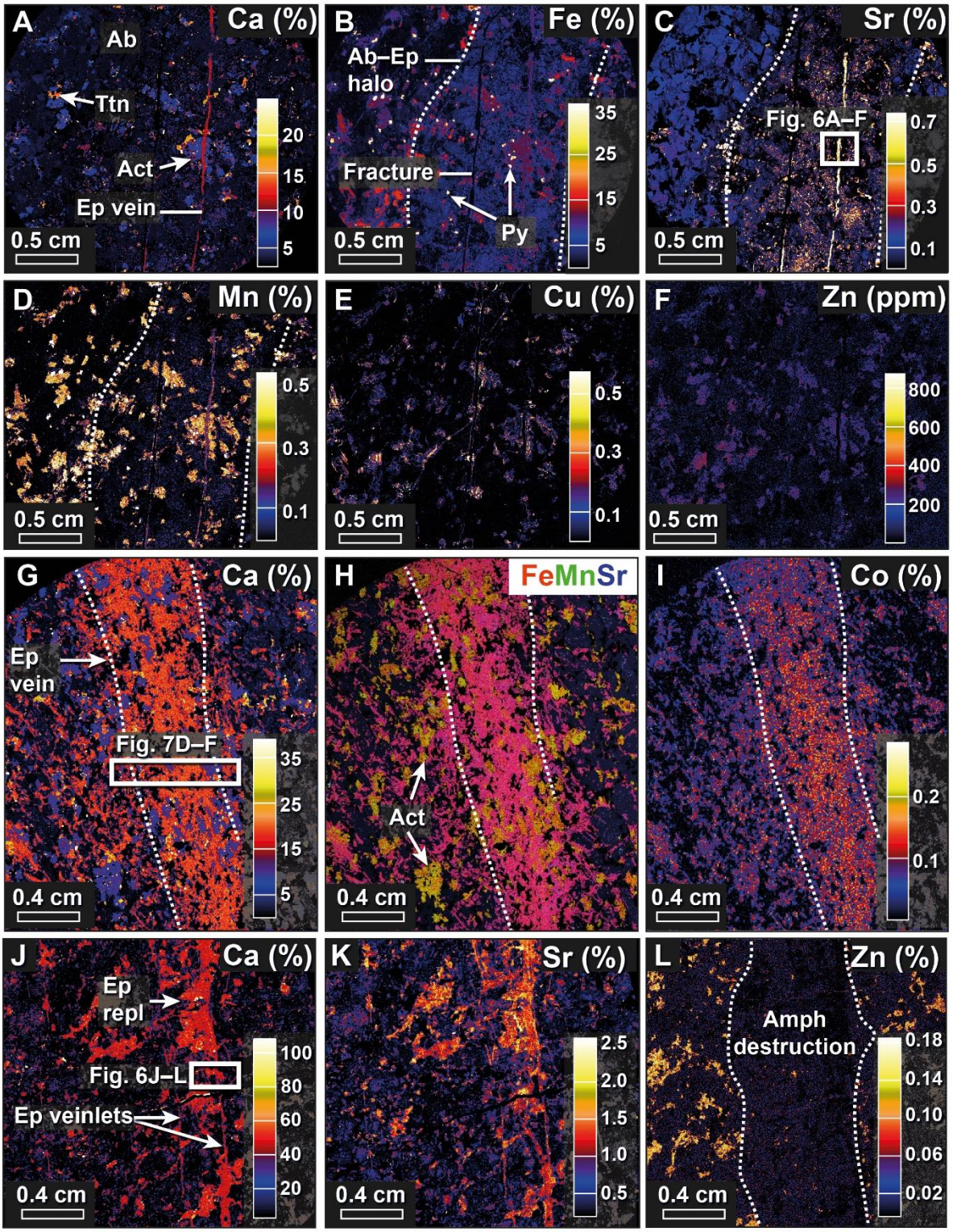
A
Ca (%)
Ab
Ttn
Act
Ep vein
20
15
10
5
0.5 cm
B
Fe (%)
Ab–Ep halo
Fracture
Py
35
25
15
5
0.5 cm
C
Sr (%)
Fig. 6A–F
0.7
0.5
0.3
0.1
0.5 cm
D
Mn (%)
0.5
0.3
0.1
0.5 cm
E
Cu (%)
0.5
0.3
0.1
0.5 cm
F
Zn (ppm)
800
600
400
200
0.5 cm
G
Ca (%)
Ep vein
Fig. 7D–F
35
25
15
5
0.4 cm
H
FeMnSr
Act
0.4 cm
I
Co (%)
0.2
0.1
0.4 cm
J
Ca (%)
Ep repl
Fig. 6J–L
Ep veinlets
100
80
60
40
20
0.4 cm
K
Sr (%)
2.5
2.0
1.5
1.0
0.5
0.4 cm
L
Zn (%)
Amph destruction
0.18
0.14
0.10
0.06
0.02
0.4 cm

Figure 5

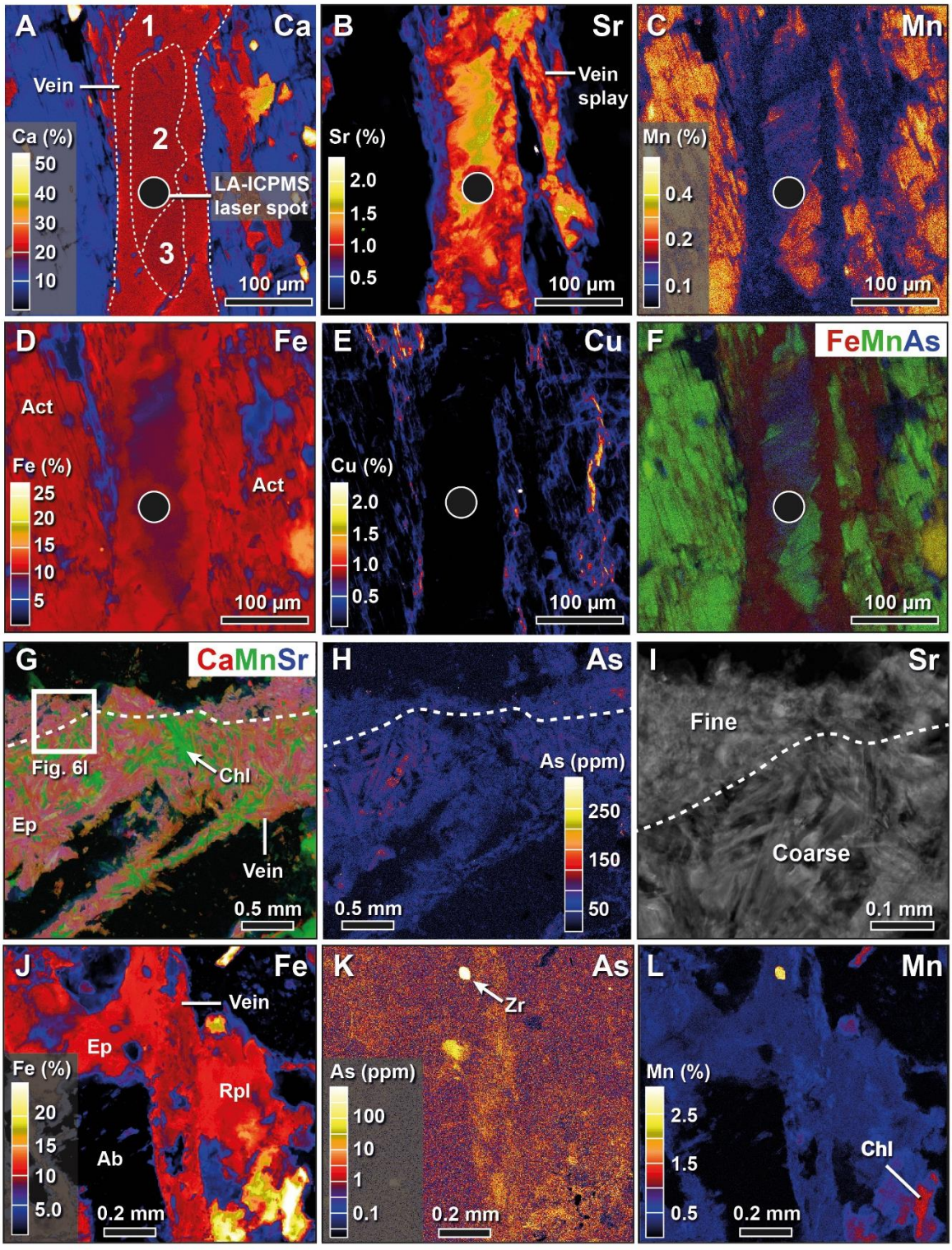
A
1
Ca
Vein
Ca (%)
50
40
30
20
10
2
LA-ICPMS
laser spot
3
100 µm
B
Sr
Vein
splay
Sr (%)
2.0
1.5
1.0
0.5
100 µm
C
Mn
Mn (%)
0.4
0.2
0.1
100 µm
D
Fe
Act
Fe (%)
25
20
15
10
5
Act
100 µm
E
Cu
Cu (%)
2.0
1.5
1.0
0.5
100 µm
F
FeMnAs
100 µm
G
CaMnSr
Fig. 6l
Chl
Ep
Vein
0.5 mm
H
As
As (ppm)
250
150
50
0.5 mm
I
Sr
Fine
Coarse
0.1 mm
J
Fe
Vein
Ep
Fe (%)
20
15
10
5.0
Rpl
Ab
0.2 mm
K
As
Zr
As (ppm)
100
10
1
0.1
0.2 mm
L
Mn
Mn (%)
2.5
1.5
0.5
Chl
0.2 mm

Figure 6

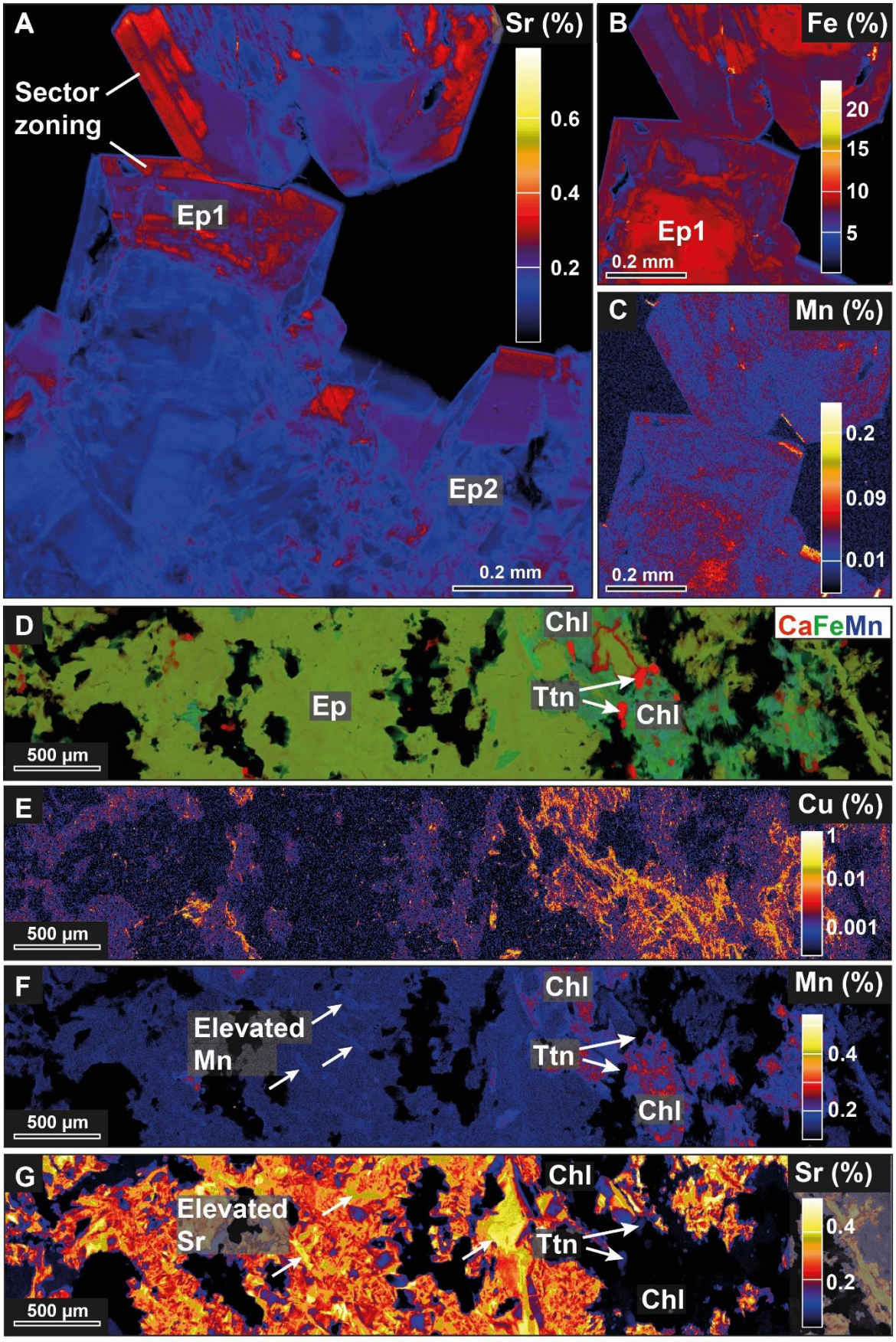
A
Sr (%)
Sector zoning
Ep1
Ep2
0.6
0.4
0.2
0.2 mm
B
Fe (%)
20
15
10
5
Ep1
0.2 mm
C
Mn (%)
0.2
0.09
0.01
0.2 mm
D
Chl
CaFeMn
Ep
Ttn
Chl
500 µm
E
Cu (%)
1
0.01
0.001
500 µm
F
Chl
Mn (%)
Elevated Mn
Ttn
Chl
0.4
0.2
500 µm
G
Chl
Sr (%)
Elevated Sr
Ttn
Chl
0.4
0.2
500 µm

Figure 7

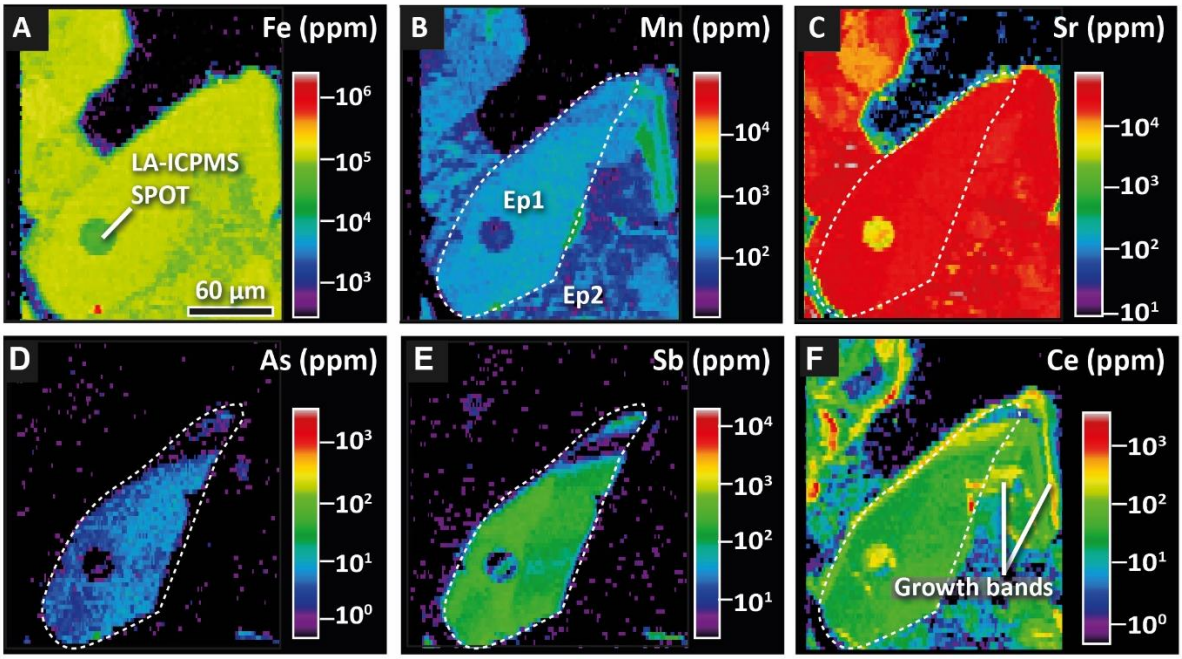

Figure 8

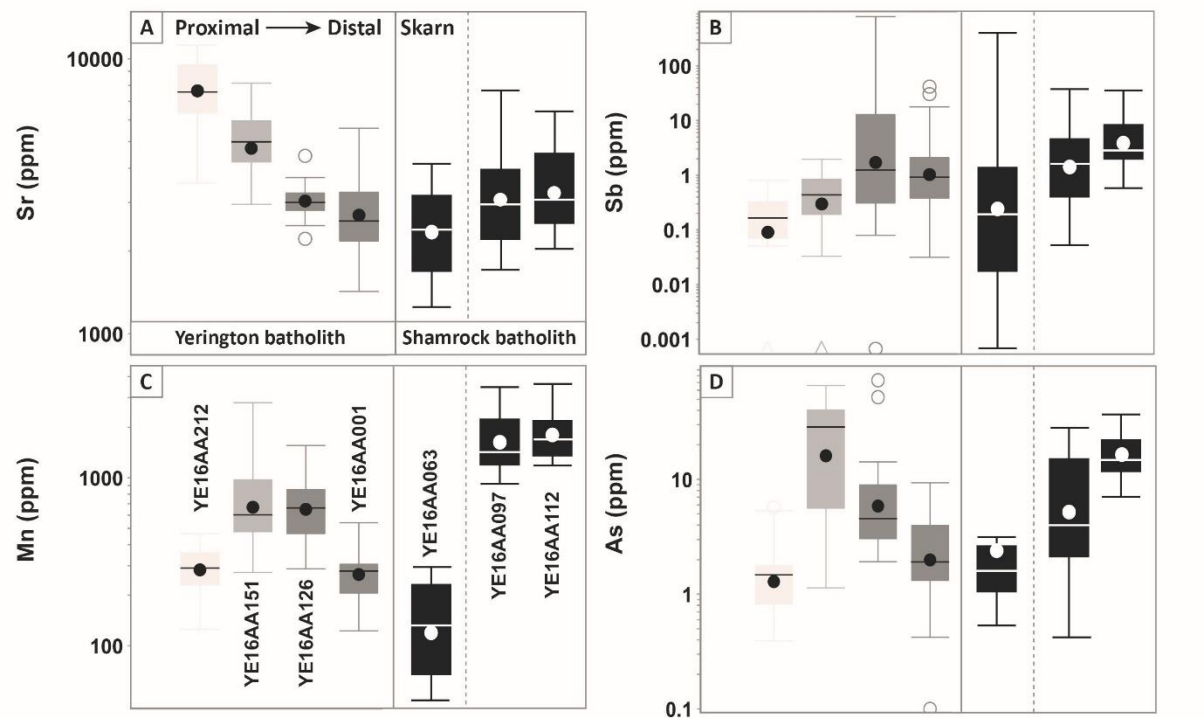

Figure 9

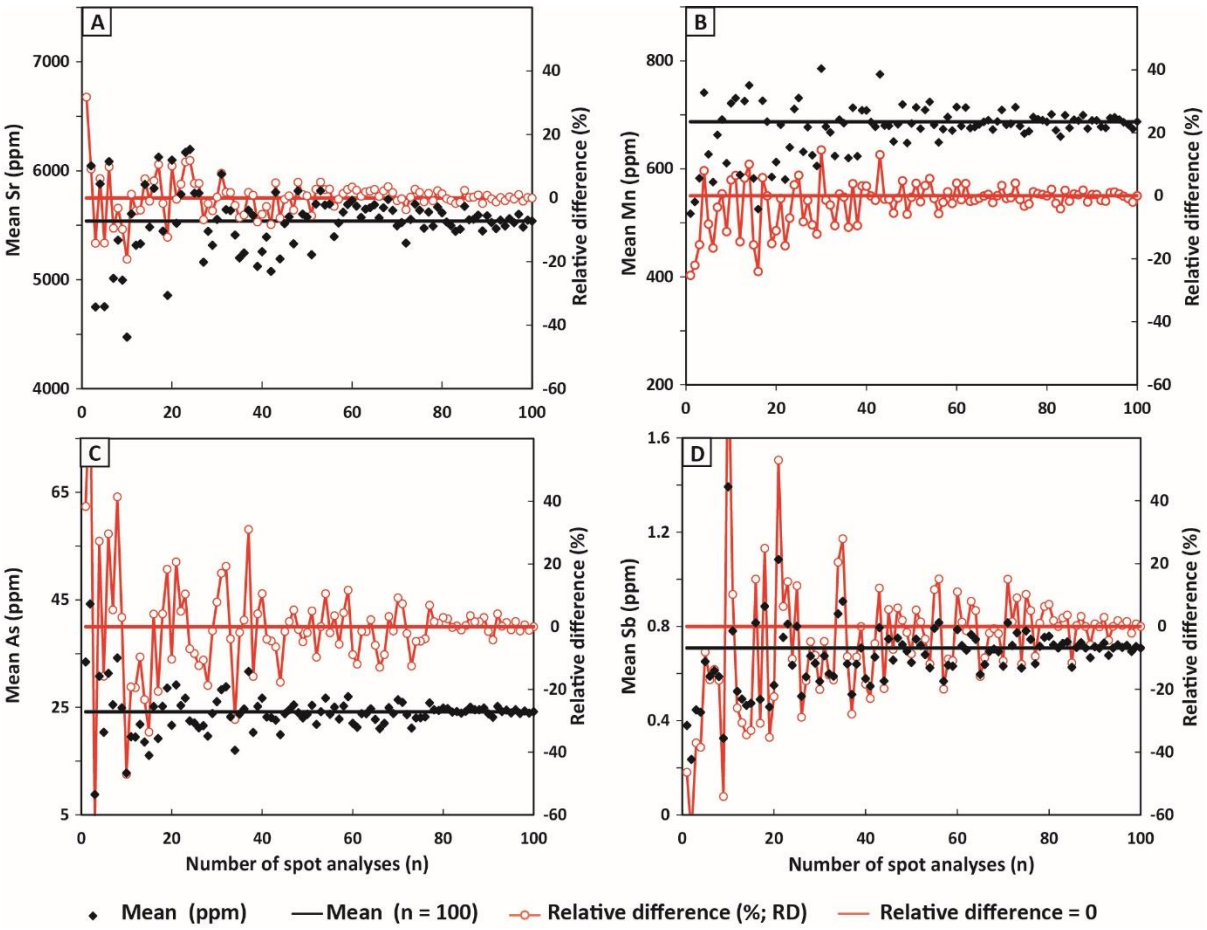
A
B
C
D
Mean Sr (ppm)
Mean Mn (ppm)
Mean As (ppm)
Mean Sb (ppm)
Relative difference (%)
Number of spot analyses (n)
Mean (ppm)
Mean (n = 100)
Relative difference (%; RD)
Relative difference = 0

Figure 10

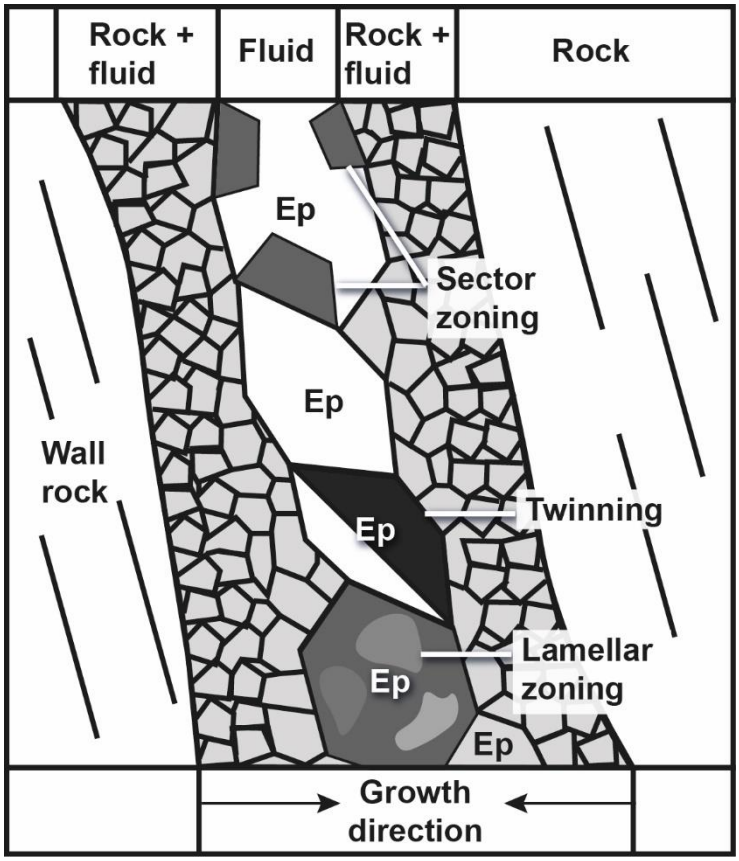
Rock + fluid
Fluid
Rock + fluid
Rock
Ep
Sector zoning
Ep
Wall rock
Twinning
Ep
Lamellar zoning
Ep
Ep
Growth direction

Figure 11

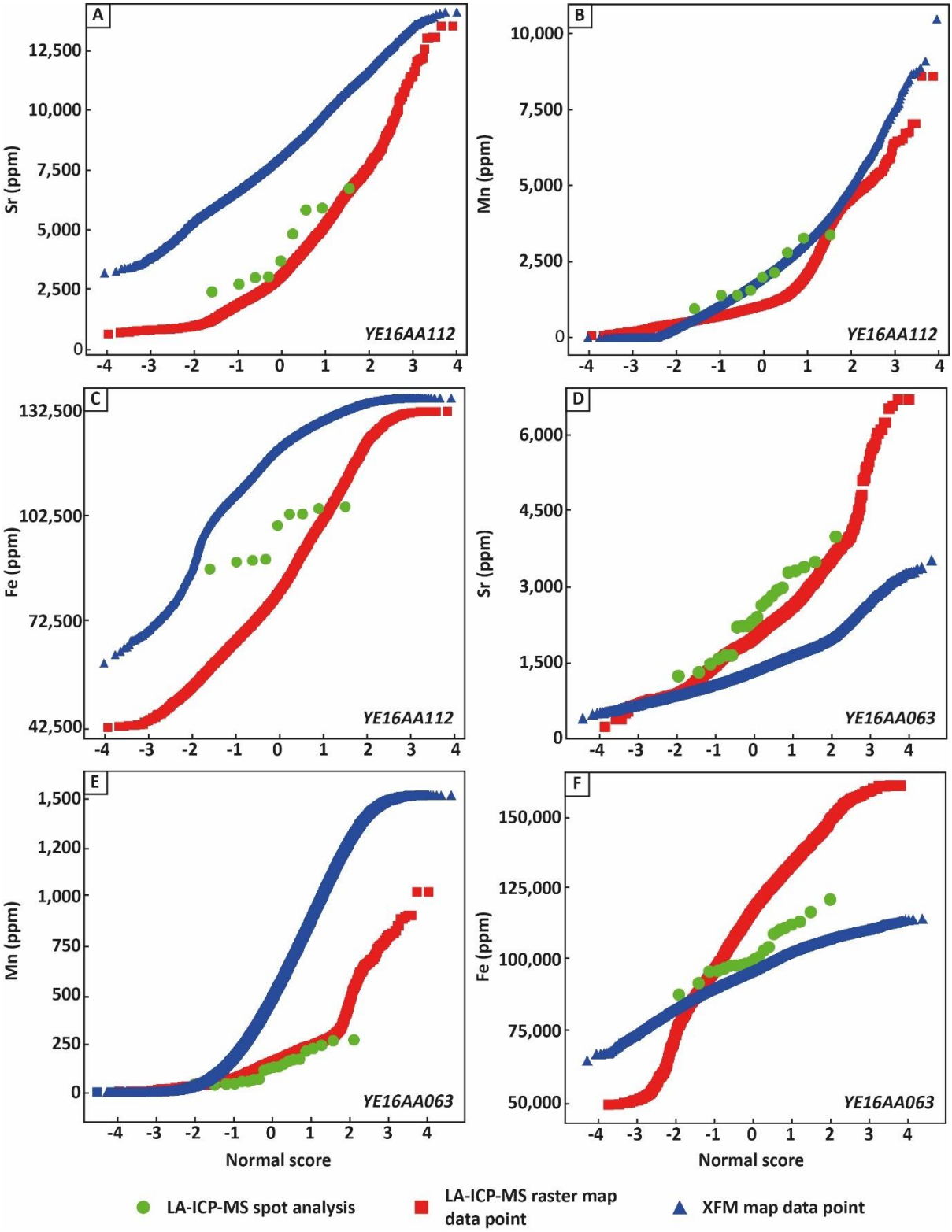
A
Sr (ppm)
12,500
10,000
7,500
5,000
2,500
0
YE16AA112
B
Mn (ppm)
10,000
7,500
5,000
2,500
0
YE16AA112
C
Fe (ppm)
132,500
102,500
72,500
42,500
YE16AA112
D
Sr (ppm)
6,000
4,500
3,000
1,500
0
YE16AA063
E
Mn (ppm)
1,500
1,200
1,000
750
500
250
0
YE16AA063
F
Fe (ppm)
150,000
125,000
100,000
75,000
50,000
YE16AA063
-4 -3 -2 -1 0 1 2 3 4
Normal score
LA-ICP-MS spot analysis
LA-ICP-MS raster map data point
XFM map data point

Figure 12